

# 2D and 3D thermoelastic phenomena in double wall transpiration cooling systems for gas turbine blades and hypersonic flight

Christos Skamniotis and Alan C.F. Cocks

Department of Engineering Science, University of Oxford, Parks Road,  
Oxford OX7 6DP, UK

## ABSTRACT

Double wall transpiration cooling (DWTC) systems allow the operating temperature of gas turbines to be increased beyond current levels, promising further enhancements in engine efficiency and a reduction in fuel consumption and emissions. Alongside the outstanding cooling performance of DWTC systems, there are structural integrity implications that need to be evaluated. Our theoretical and Finite Element (FE) analysis here determine thermal stresses arising in a range of double wall configurations in two-dimensional (2D) and three-dimensional (3D) space. The 3D geometric effects of wall spacing, wall thickness ratio, connecting pedestal spacing between the walls and pedestal thickness are interpreted based on considerations on 2D idealisations. We highlight that although an inner cool wall may be essential for applying internal impingement cooling in the system to enhance its aerothermal performance, at the same time the inner wall increases compression in the hot outer wall, due to the kinematic constraint that the two walls must extend equally. As a result, the critical compressive stresses in the hot wall can be relieved by using a thinner inner wall. Our study determines the essential nominal stress fields that drive stress concentrations and associated local creep-plasticity-fatigue at critical features in DWTC systems, such as effusion holes and pedestals.

**Keywords:** Double wall transpiration cooling, creep-fatigue, gas turbine blades, finite elements, thermal stresses, stress concentration factor.

## Nomenclature

### Abbreviations

DWTC = double wall transpiration cooling

FE = Finite elements

2D = two-dimensional

3D = three-dimensional

MPC = multipoint constraint

DOF(s) = degree(s) of freedom

### Symbols

#### Thermal

$T_{max}$  = temperature at outer wall hot surface (K)

$T_{min}$  = minimum temperature at inner surfaces (K)

$T_0$  = reference/room temperature (K)

$\Delta T$  = thermal difference (K)

#### Structural

$R$  = radius of curvature (mm)  
 $t$  = wall thickness (mm)  
 $s$  = wall arc-length (mm)  
 $D$  = diameter (mm)  
 $H$  = wall spacing/pedestal height (mm)  
 $L$  = pedestal spacing (mm)  
 $\mathcal{H}$  = distance between wall centrelines  
 $\rho$  = pedestal-wall fillet radius (mm)  
 $\varrho$  = longitudinal pedestal fillet radius (mm)  
 $\psi$  = unit cell angle (rad)  
 $I$  = second moment of area (mm<sup>4</sup>)

#### Material

$E$  = Elastic Modulus (MPa)  
 $\nu$  = Poisson's ratio  
 $\alpha$  = thermal expansion coefficient (m/m·K)  
 $k$  = thermal conductivity (W/m·K)

#### Mechanical

$u$  = displacement (mm)  
 $\varphi$  = rotation (rad)  
 $\kappa$  = total bending curvature (1/mm)  
 $\varepsilon$  = total engineering normal strain  
 $\mathcal{N}$  = membrane force (N)  
 $N$  = membrane force per unit length (N/mm)  
 $M$  = bending moment per unit length (N·mm/mm)  
 $Q$  = shear force per unit length (N/mm)  
 $\sigma$  = maximum absolute principal (Cauchy) stress (MPa)  
 $\sigma_j$  = (Cauchy) stress component (MPa) in  $j$  direction  
 $\sigma_1$  = maximum principal stress  
 $\sigma_2$  = medium principal stress  
 $\sigma_3$  = minimum principal stress  
 $SCF$  = stress concentration factor

### **Accents – superscripts**

$\hat{\phantom{x}}$  = quantity normalised over outer wall thickness (dimensionless)  
 $\bar{\phantom{x}}$  = dimensionless position

### **Subscripts**

$1$  = outer (hot) wall property  
 $2$  = inner (cooler) wall property  
 $P$  = pedestal property  
 $f$  = fillet property  
 $out$  = wall outer surface property  
 $in$  = wall inner surface property

$i$  = wall identifier  
 $j$  = direction identifier  
 $y$  = position through wall thickness (mm)  
 $\theta$  = circumferential axis/direction  
 $z$  = longitudinal axis/direction  
 $r$  = radial axis/direction

# 1. Introduction

Gas turbine and hypersonic flight applications rely heavily on cooling [2-5]. The way in which a cooling system maintains temperature, often determines the balance between the efficiency of such applications and the life of critical structural components [3]. Recent recognition of environmental damage levels associated with carbon dioxide emissions and fuel consumption related to aviation is an additional, timely aspect that can also be addressed through better cooling [6-9]. This is because improved thermal protection allows for higher gas temperatures to operate in the core of turbines, which increases engine efficiency and specific power output [10]. Indeed, this idea is well established in engine design [2, 11] and over the last fifty years has contributed to the rise of the operating engine core temperature more than other relevant technological advances related to nickel superalloys, thermal barrier coatings and manufacturing [12, 13]. Consequently, exploring increasingly sophisticated thermal protection systems is key for addressing emerging environmental and energy challenges [11, 13].

Currently, effusion and transpiration are cutting edge external cooling strategies that already allow operating temperatures beyond the material limits of engine core components [4, 8, 14]. This is primarily due to the large decrease in the temperature driving heat transfer from the mainstream hot gas flow onto the metal, which is achieved by ejecting internal coolant through effusion/film holes at the exterior surface of the component, in a directed manner, such that a protective cool film is formed [5, 15, 16]. Double wall transpiration cooling (DWTC) is a more advanced concept which enables the combination of the above external cooling technique with internal cooling features, consisting of coolant impingement and pedestals; the role of these internal features can be demonstrated through the double wall system presented by Murray et al [17] for an aerofoil, shown here in Fig 1a. Specifically, pedestals connect the two walls and simultaneously offer conductive cooling of the hot outer skin, while impingement holes eject high speed coolant jets onto the inner surface of the outer wall, thus promoting convective cooling. The impingement phenomenon has been suggested to result in the highest local increase in convective heat transfer coefficients amongst all the available methods of promoting heat transfer [18, 19]. Moreover, the pedestals, as well as provide a path for heat conduction, also enhance turbulence in the coolant flow patterns between the walls, enhancing further these convective heat transfer coefficients [4, 13]. As a result of the above phenomena, numerical simulations suggest that DWTC provides higher overall convective efficiency and cooling effectiveness in comparison to other available thermal protection strategies [10, 13, 15].

Although the excellent cooling/aerothermal performance of double wall transpiration systems has been well demonstrated in the open literature [3, 4, 13, 18], their thermomechanical performance and sensitivity to potential creep-fatigue failure is less explored [20]. Concerns regarding the unknown magnitude of thermal stresses that may arise in the rather complex double wall configurations are suggested to have delayed their practical implementation [4, 21, 22], not to mention further complexity induced by geometric non-linearities i.e. effusion-impingement holes [22], as well as

material non-linearities i.e. creep-plastic strain accumulation [6, 23, 24]. For critical engine hot stage components, such as conventional turbine rotor blades, the major importance of thermal stresses over mechanical (centrifugal/inertial) stresses [25-27] and aerodynamic bending (gas bending) stresses has been shown [4, 22, 28]. However, information for non-conventional double wall configurations is limited to the reports by Murray et al [4], Elmukashfi et al [29] and the recent work by the authors [20].

Murray et al [4] performed coupled thermomechanical-aerothermal 3D analysis in large scale flat double wall effusion cooling configurations using simple structural constraints. The study identified that significant thermal stresses mainly arise by a temperature gradient through the thickness of the outer wall as well as by the average temperature difference between the two walls which are mechanically coupled by the pedestals. The latter was studied in more depth by Elmukashfi et al [29] who derived both FE and plate theory solutions for 2D and axisymmetric flat double wall geometric idealisations, that described the nature of the thermal stress field as a function of geometry. The sensitivity of thermal stresses as a function of primary geometric features, temperature field perturbations as well as heat transfer, coolant flow constants i.e. Biot and Reynolds numbers, was also investigated.

Recently [20], we presented more detailed analytical (beam/plate theory) and FE 2D solutions which accounted for primary geometric characteristics relevant to turbine blade components (e.g. Fig 1a), such as the geometric curvature and the closed cross sectional profile of cylindrical-like bodies. By using the idealised scenario of a prescribed thermal gradient through the thickness of the outer wall, we showed that analytical solutions can guide a straightforward initial geometric optimisation in order to modify the thermal stress field in favour of various critical features of the double wall system: principally, the effusion/impingement holes and the fillet corners between the pedestals and walls. Stresses at holes were found to be equal to the nominal stresses in the absence of holes, scaled by a stress concentration factor, which highlighted that understanding and manipulating nominal thermal stresses is of vital importance for reducing the actual stresses at these critical locations.

This study aims to verify whether theoretical analysis and geometry-stress relations determined for 2D idealisations also apply in 3D double wall geometries, as well as identifying additional effects that come into play in 3D. We will then be able to assess whether 2D calculations can guide the interpretation of larger scale 3D simulation data and whether the 2D observed trends in behaviour can be used to reduce the range of 3D configurations that needs to be studied in the conceptual and post-conceptual design stages [30]. Knowledge of such aspects is important for accelerating the entire design process, considering the severe increase of computational cost with increasing 3D FE mesh size, particularly when material creep-plasticity non-linearities and/or transient cyclic loading histories are being modelled [31]. Often, 3D thermoelastic stress data in the elastic regime can provide the essential input parameters in subsequent shakedown and creep-fatigue life calculations [23, 32-40]. Such calculations provide the means for improving and/or balancing thermodynamic cycle efficiency and service life, in high temperature double wall components in gas turbines [40, 41] as well as other technologies [15, 42-44].

In Section 2 we report stress results for thermal loading of a typical single wall and double wall gas turbine blade. These results justify our geometric idealisation for the double wall system, which is described together with the temperature field idealisation; based on these idealisations we then present a theoretical thermoelastic stress analysis and describe our FE modelling strategies. Thereafter, Section 3 presents 2D and 3D results, followed by a presentation of the various effects of geometry on stresses at critical locations.

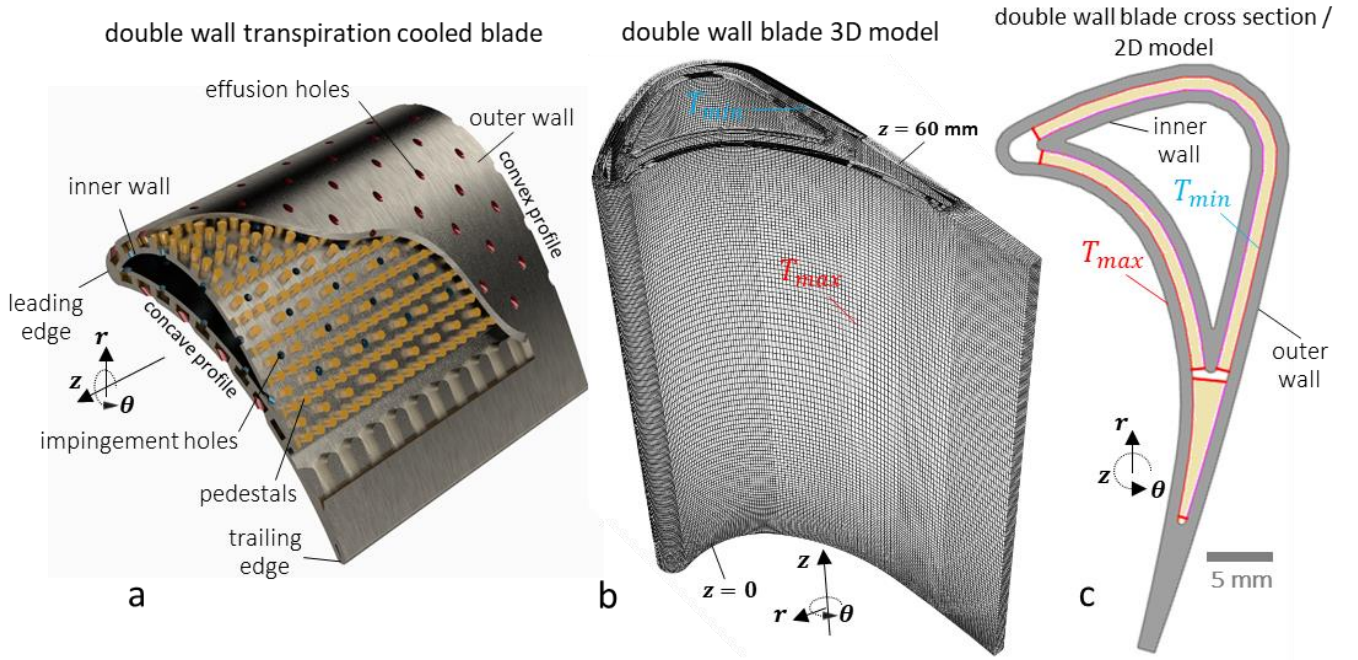


Figure 1. Double wall gas turbine blade configurations. Images show: (a) a double wall transpiration cooled gas turbine blade presented in [14], (b) 3D FE model mesh of a double wall blade, based on the root section of a NASA blade reported in [1], (c) cross section of the double wall 3D model shown in (b), with wall coupling constraint denoted in yellow; the cross section is used in 2D simulations based on generalised plane strain elements.

## 2. Methods

### 2.1 Preliminary study of the large-scale response of a turbine blade

#### 2.1.1 Gas turbine blade model

In order to be able to analyse 2D and 3D phenomena in a typical transpiration cooled double wall system (Fig 1a), it is essential to consider a representative unit cell with appropriate boundary conditions. To cover a range of potential double wall configuration scenarios, the effect of different boundary conditions on the membrane forces and bending moments that are generated in the two walls during thermal loading, will be addressed in this study. Through a preliminary study, we also identify the boundary conditions that are most relevant to a typical gas turbine blade; this will indicate whether our representative unit cell can be used in the design of double wall gas turbine blades.

FE simulations are performed on 2D-3D single and double wall blade configurations based on the NASA Energy Efficient Engine (E<sup>3</sup>) high pressure single wall turbine blade, originally reported by Thulin et al [1] and later analysed by Cunha et al [45]. Our configurations are generated in the commercial finite element code ABAQUS CAE [31] as follows. We initially reconstruct the cross-sectional profile of the outer edge of the blade by constructing splines along 20 coordinates that correspond to the root section of the NASA blade [1]; the root section is selected because it involves larger curvatures at both the convex (suction side) and concave (pressure side) surfaces of the blade than any other section along the  $z$  axis of the actual blade geometry [1]. In this manner, we examine the case where the potential curvature effects on the thermoelastic stress state are maximum. Note

also that further to the thermal loading studied here the root section in practise often experiences the most severe centrifugal stresses and therefore is of high engineering importance [25, 46]. The inner edge profile is then obtained through an inward offset of the curved outer edge by 1 mm; for the double wall 2D configuration shown in Fig 1c, the inner wall edges are obtained in a similar manner i.e. via two consecutive offsets by 1mm. The above implies that 1 mm is consistently used for wall thicknesses and wall spacing. The details of the geometry in Fig 1c, i.e. filleted corners and exact perimeter of the inner wall, are chosen to agree with the double wall configuration reported by Ngetich [10], and are not significant for our analysis here. An extrusion of the 2D profile of Fig 1c through 60 mm produces the 3D double wall model of Fig 1b. We ignore the actual geometric twist of the cross-sectional profile around the  $z$  axis (available in [1]), as well as the actual tapering i.e. decrease of wall thickness along  $z$ , as here we are interested in understanding the first order characteristics of the thermal stress field in double wall blades and investigating whether these characteristics can be reproduced by applying appropriate boundary conditions in a repeating unit block that is cut out from a given region of the blade. Note also that the slight degree of twist was introduced in [1] for a single wall blade, in order to find the best balance between gas bending stresses and centrifugal stresses. In emerging double wall blade systems, the gas bending stresses can be minor (due to the drastic increase of effective second moment of area of blade) and therefore a geometric twist may or may not be necessary.

Steady-state coupled temperature-displacement analyses are performed based on the ABAQUS Newton-Raphson scheme. In 3D (Fig 1b) we use 8-node thermally coupled brick, trilinear displacement and temperature elements (ABAQUS code: C3D8T), whereas in 2D (Fig 1c) we use 4-node generalized plane strain, thermally coupled quadrilateral, bilinear displacement and temperature, reduced integration, hourglass controlled, elements (ABAQUS code: CPE4RT). A minimum of 30 elements through the wall thicknesses was found to give results that change insignificantly with further mesh refinement; this approximately corresponded to a total of 1,600,000 elements for the 3D double wall model in Fig 1b. Material properties include the following for CMSX-4 nickel-based superalloy [47, 48] for temperatures in the range 300–800 K: elastic modulus,  $E = 120000$  MPa, Poisson's ratio,  $\nu = 0.3$ , thermal expansion coefficient,  $\alpha = 1.2 \cdot 10^{-5}$  m/m·K and thermal conductivity,  $k = 14$  W/m·K. In both 2D and 3D cases and for both single and double wall geometries, thermal loading is applied by prescribing a high temperature,  $T_{max} = 1000$  K, uniformly along the outer edge/surface of the outer wall (denoted in Figs 1b-c), whilst postulating a low temperature,  $T_{min} = 300$  K, along the interior edge/surface of the outer wall, in order to induce the thermal difference,  $\Delta T = T_{max} - T_{min}$ ; thermal expansions are calculated with respect to a reference temperature of  $T_0 = 300$  K. Thermoelastic stresses here depend solely on  $\Delta T$ , which allows for using arbitrary values for  $T_{max}$ ,  $T_{min}$  and  $T_0$ . The above temperatures In both 2D and 3D, the connectivity of walls through pedestals is modelled here via enforcing a 'tie' constraint which prevents relative translation/rotation between each node lying at the inner edge/surface of the outer wall and its corresponding adjacent node lying in the inner edge/surface of the inner wall. The constraint is applied in a uniform manner, as denoted by the yellow colour in Fig 1c, with the exception that some regions, i.e. near the leading edge, where no coupling is applied for the purpose of consistency with the system presented by Ngetich [10]. Emphasis here is only given to regions where the outer and inner walls are coupled and are away from the ends. In 3D (Fig 1b), we additionally constrain all the translations/rotations of all the nodes lying on the bottom plane,  $z = 0$ , i.e. fixed boundary, while nodes on the top plane,  $z = 60$  mm, are free.



# stress field in single/double wall 3D blade

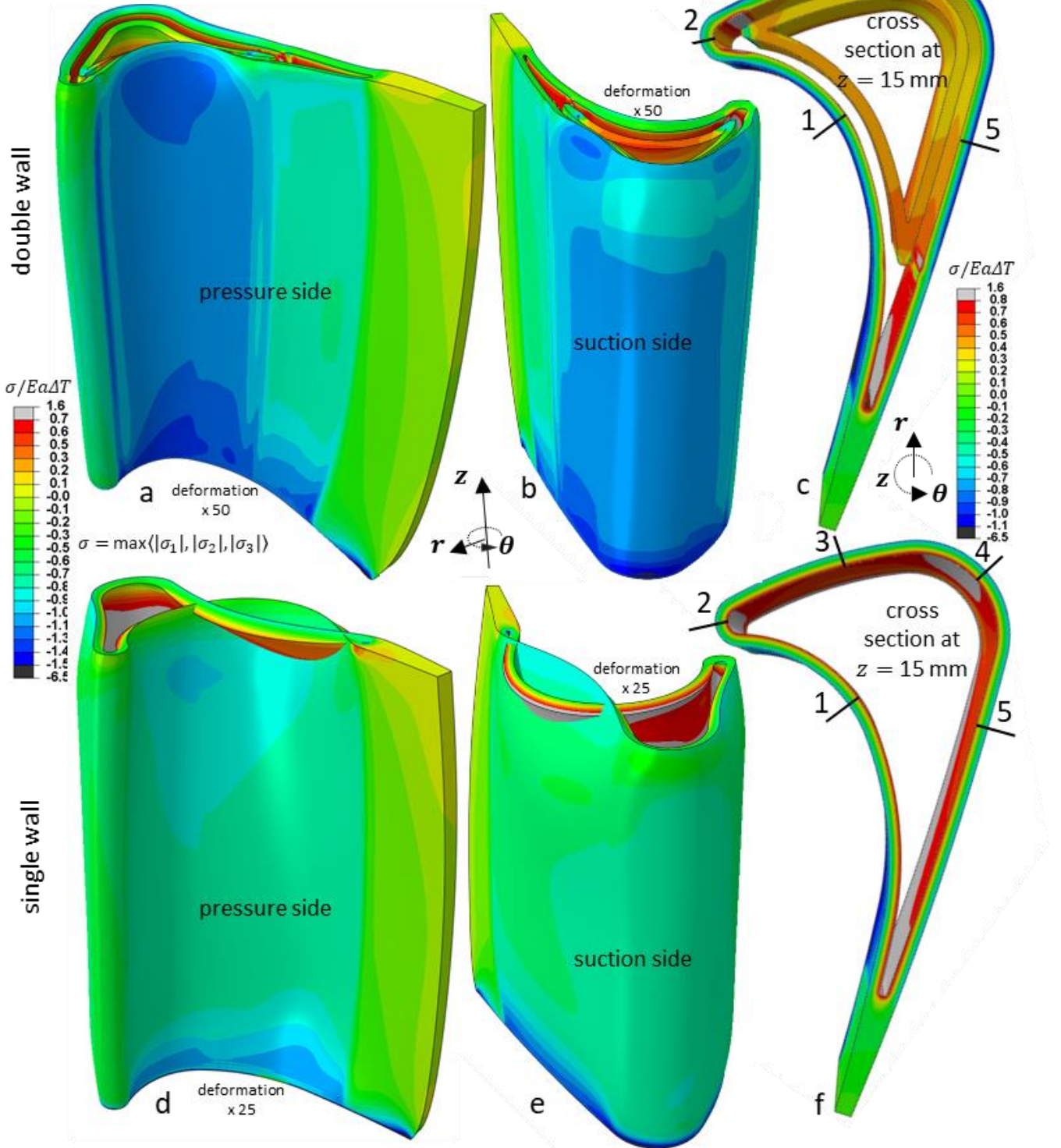


Figure 2. Stress fields for 3D analyses of thermally loaded gas turbine blades with single and double walls; contours show maximum absolute principal stress normalised with respect to  $Ea\Delta T$ . Wall thicknesses and a wall spacing of 1 mm are used. Images show: (a) pressure side of a double wall blade; structural kinematics are highlighted by using a deformation scale factor of 50, (b) suction side of double wall blade shown in (a), (c) sectioned view of the double wall blade shown in (a-b) at 1/4 of the total length of blade; no deformation scaling is applied here, (d) pressure side of single wall blade; a deformation scale factor of 25 is used here, (e) suction side of single wall blade shown in (d), (f) sectioned view of single wall blade shown in (d-e) at the plane  $z = 15 \text{ mm}$ .

### 2.1.2 Stresses predicted by 2D and 3D analyses of a gas turbine blade

The stress field from the 3D analysis of the gas turbine blade is summarised in Figs 2a-f; these show maximum absolute principal stresses,  $\sigma = \max(|\sigma_1|, |\sigma_2|, |\sigma_3|)$ , normalised with respect to the thermal loading factor,  $E\alpha\Delta T$ . Extreme compressive stresses near the fixed bottom boundary (at  $z = 0$ ) are not a concern in our analysis here because these stresses are generated by the application of the fixed boundary condition in combination with the absence of rounded corners at the bottom of the walls; in practise, the geometric characteristics and underlying structural constraints near the root of a turbine blade are different [41, 49, 50]. The same applies near the free end of the turbine rotor blades, where in reality a cap would typically exist [1, 51]; note that the latter may be necessary to prevent coolant outflow along the principal blade axis,  $z$ . Depending on the flexural stiffness of the cap, the response near the free end of the blades could change considerably with respect to the results of Figs 2a-b and Figs 2d-e. Here we only analyse the steady state stress field which occurs away from the fixed bottom boundary (at  $z = 0$ ) and away from the top free ends of the walls (at  $z = 60$  mm). A major feature of this steady state stress field for both the single (Figs 2d-e) and double wall blade (Figs 2a-b), is that it is effectively independent of position  $z$  away from the boundaries.

We analyse the steady state stress field at the representative section/plane,  $z = 15$  mm, for which the corresponding stress contours are illustrated in Fig 2c and Fig 2f for the double and single wall cases, respectively. For the same plane, we also plot in Fig 3, the stresses at the locations of interest 1-5 (denoted in Figs 2c, f), for both the 3D and 2D analyses, and compare them with theoretical solutions which will be derived in Section 2.3. Near the locations of interest, 1, 3, 4, 5 (denoted in Figs 2c, f), where the kinematic ‘tie’ constraint is uniformly applied between the two walls (see Fig 1c), the stresses are found to effectively only exist along the two principal in-plane directions of the walls: along the circumferential (tangential) direction of the walls and along the axial,  $z$ , direction of the blade. Out-of-plane stresses through the wall thickness are found to be negligible. The important feature for the above locations is that the first and second principal stresses in the plane of the walls, are approximately equal i.e. an equibiaxial state, implying that equal bending moments and membrane forces are generated in the two directions. This in turn suggests that the same type of structural constraint applies in the two directions. In this regard, Fig 3 shows that for the case of a single wall blade, the compressive and tensile stresses at the outer and inner wall surfaces, respectively, are almost identical (for locations 1, 3, 4, 5) i.e. a symmetric distribution through the wall thickness; the latter indicates that membrane forces are zero, which is consistent with the case of a long cylindrical thin wall subjected to a thermal difference,  $\Delta T$ , between its outer and inner surfaces [52]. As a result, for locations 1, 3, 4, 5, Fig 4 shows an agreement between the compressive/tensile stresses in the single wall blade and the theoretical solution,  $\sigma = (1/2)E\alpha\Delta T/(1 - \nu)$ , for a long cylinder with a thin wall. The theoretical solution is based on classical plate theory i.e. assumption of a flat plate and postulates that the total bending curvatures (and thus rotations) about the two principal directions are zero; this explains why agreement is also found between the results of the 3D FE analysis and the results of the 2D FE analysis based on generalised plane strain elements (see Fig 3).

With regards to the double wall blade, agreement is found between the FE results and the analytical theoretical solution presented in Section 2.3.5. The main characteristic is that in addition to the self-imposed constraint associated with zero bending curvatures/rotations in two directions, the presence of the inner wall imposes an additional constraint that the two walls extend equally in the axial,  $z$ , direction. This generates a significant compressive membrane force in the outer wall, such that in Fig



3 the compressive stresses in the outer surface increase and the tensile stresses in the inner surface decrease with respect to the stresses in the single wall blade (also compare contours between Fig 2c and 2f). Both for the single and double wall cases, the theoretical-FE agreement in Fig 3 is only shown to break down in regions where the wall(s) is/are highly curved, such as location 4 and especially near the leading edge i.e. location 2. The large curvature near location 2 is specifically shown to decrease the compressive stress at the outer surface and increase the tensile stress at the inner surface of the outer wall. It has been shown [20] that the above phenomenon is triggered by the fact that locally at the leading edge, the outer compressive side of the wall is considerably longer than the inner tensile side, giving rise to a non-linear stress distribution through the wall thickness; these non-linear effects diminish at regions of small curvature i.e. locations 1, 3, 5, for which flat plate theory is shown to be valid in Fig 3. For these regions the results of this section indicate that the cylindrical double thin wall geometry provides an accurate idealisation of the gas turbine blade system.

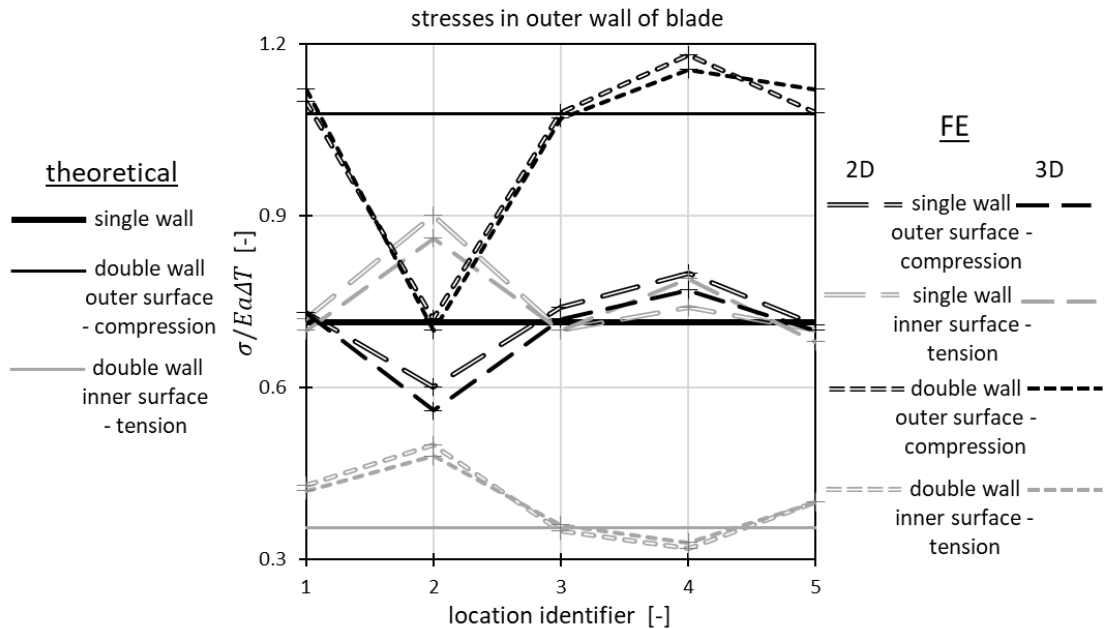


Figure 3. Comparison of theoretical-FE stress solutions at the 5 distinct locations of the outer wall, denoted in Figs 2c,f; the corresponding gas turbine blade models are shown in Figs 1b-c. Location 1 lies within the pressure side of the blade, where the outer surface is concave (see Fig 2c); location 2 represents the leading edge where the convexity of the outer surface changes and the walls are highly curved (see Fig 2c); locations 3, 4 and 5 are relevant to the suction side where the outer surface is convex (see Fig 2c).

## 2.2 The unit cell - geometric and temperature field idealisations

We now adopt the cylindrical wall idealisation in order to investigate the details of the thermal stress field when the walls are coupled by pedestals (instead of the kinematic ‘tie’ constraint used in Section 2.1.1), as for example in the system of Fig 1a. Specifically, we consider the periodically repeating unit cell shown in Fig 4a, which represents two concentric cylindrical thin walls (wall 1, 2), with external radius of curvature,  $R$ , connected by an array of cylindrical pedestals; a quarter of the symmetric geometry is analysed, as shown in Fig 4b, producing the  $r - z$  bisectonal 2D profile in Fig 4c and the  $r - \theta$  profile in Fig 1d.

We assume that effusion/impingement holes are absent. Stress concentrations at holes through the walls in simplified double wall geometries have been recently shown [20] by the authors to essentially scale with the nominal stresses that occur in the absence of the holes, multiplied by a stress concentration factor,  $SCF$ . Holes were also found to cause additional, more complex local effects associated with the interaction of  $SCFs$  between the hole and pedestal. In order to provide a clear and systematic understanding of the underlying thermal stress field in the absence of the above effects, we omit holes in this study, and instead emphasise the nominal stresses that arise at the location of the effusion hole, but in the absence of the hole. The detailed effect of a hole, its orientation with respect to the plane of the wall, and interactions with a pedestal fillet are considered in later study [53]. Regarding the temperature field idealisation, this involves a uniform thermal gradient,  $\Delta T = (T_{max} - T_{min})/t_1$ , through the thickness,  $t_1$ , of the outer wall, based on a prescribed uniform temperature,  $T_{max}$ , throughout the outer surface of the outer wall, and a uniform low temperature,  $T_{min}$ , at the internal surfaces of the system (see Fig 4b). The basis, the validity and the merits of this temperature field idealisation has been discussed in detail by Elmukashfi et al. [23], as well as by the authors in an earlier study [20].

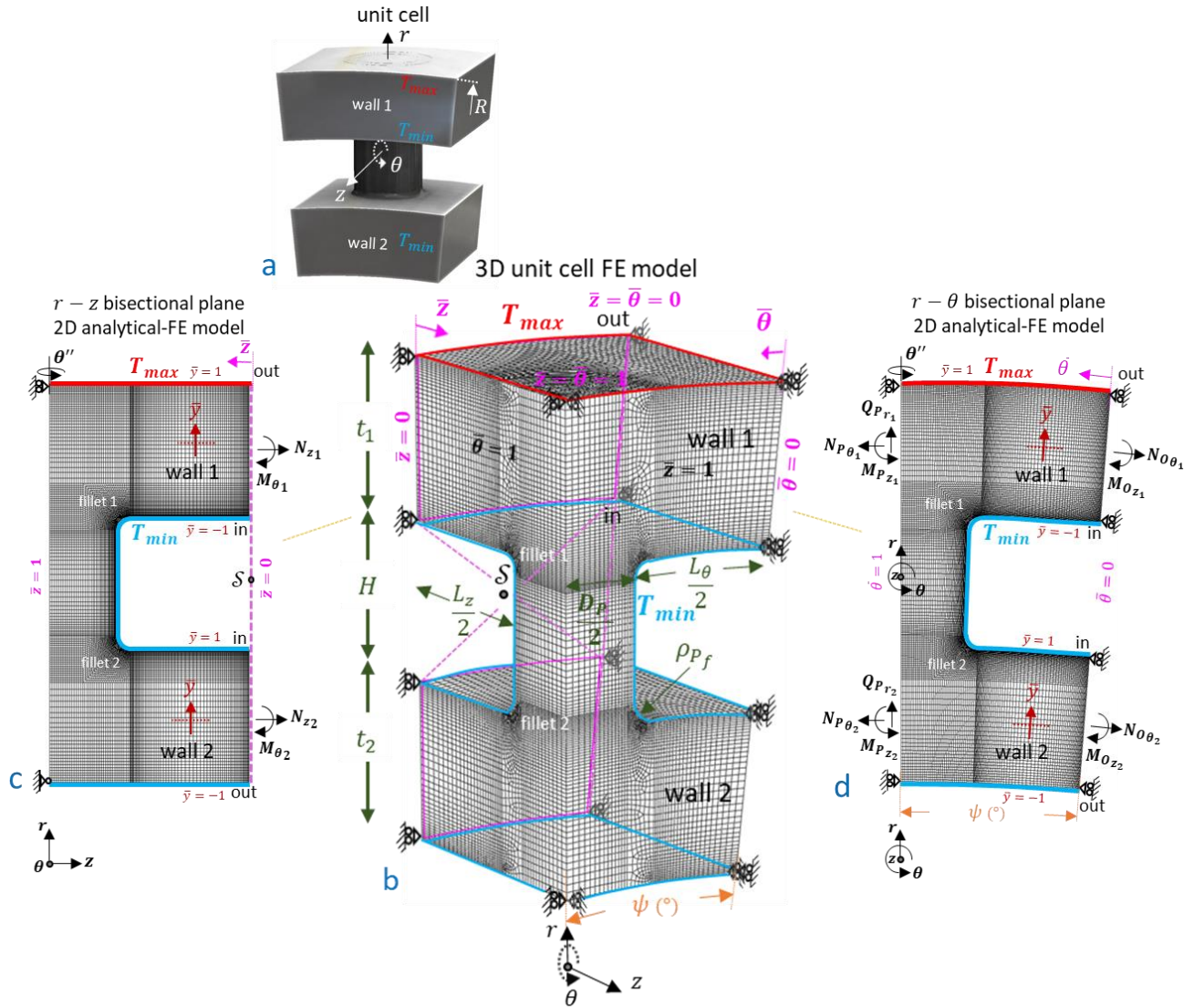


Figure 4. Summary of theoretical-FE analysis of double wall systems. Images show: (a) double wall transpiration cooled gas turbine blade (presented in [14]), (b) periodically repeating unit cell of the idealised configuration of concentric cylindrical walls connected with pedestals, (c) 3D FE model of the unit cell in (b) with dimensions, (d) 2D FE-theoretical model of the  $r-z$  bisectonal profile of the unit cell in (c), (e) 2D FE-theoretical model of the  $r-\theta$  bisectonal profile of the unit cell in (c).

The 3D unit cell geometry (Fig 4b) is defined by: the external radius of curvature,  $R$ , the outer wall thickness,  $t_1$ , the inner wall thickness,  $t_2$ , the skin spacing (pedestal height),  $H$ , the pedestal spacings,  $L_\theta$  and  $L_z$  in the circumferential,  $\theta$ , and longitudinal,  $z$  directions, the pedestal diameter,  $D_p$ , and the pedestal-wall fillet radius,  $\rho_{pf}$ ; the dimensions are often referred to in the manuscript in terms of their normalised values, whereby each of these lengths is normalised by the outer wall thickness, such that:  $\hat{R} = R/t_1$ ,  $\hat{t}_2 = t_2/t_1$ ,  $\hat{H} = H/t_1$ ,  $\hat{L}_\theta = L_\theta/t_1$ ,  $\hat{L}_z = L_z/t_1$ ,  $\hat{D}_p = D_p/t_1$ ,  $\hat{\rho}_{pf} = \rho_{pf}/t_1$ . Pedestal spacing,  $L_\theta$ , is measured at the inner surface of the outer wall i.e. radial position,  $R - t_1$ , so that the unit cell angle,  $\psi$  (rad), is  $\psi = (\hat{L}_\theta/2 + \hat{D}_p/2)/(\hat{R} - 1)$  (see Figs 4c-d), the wall centreline radii are  $R_1 = R - t_1/2$  and  $R_2 = R - t_1 - H - t_2/2$  and the corresponding wall arc-lengths in the  $\theta$  direction are  $s_1 = R_1\psi$  and  $s_2 = R_2\psi$ . The origin of the cylindrical system  $r\theta z$  in Figs 1c-e, is considered to be at the centre of geometric curvature. Dimensionless positions,  $\bar{\theta}$  and  $\bar{z}$ , ( $0 \leq \bar{\theta} \leq 1$ ,  $0 \leq \bar{z} \leq 1$ ) are used as denoted in Figs 4b-d.

We will now utilise the configurations shown in Figs 4c-d to provide a rigorous 2D theoretical analysis of potential structural constraints that arise in a range double wall geometries. We then consider the combination of different constraints in 3D space and build our 3D FE models accordingly. The theoretical calculations of the idealised 2D geometries provide a framework for the evaluation of the 3D FE calculations, while also providing important information about how the stresses are influenced by different geometric parameters.

## 2.3 Theoretical analysis of structural constraints

### 2.3.1 Internally constrained non-zero rotations in flat double walls

When two walls are connected through pedestals, compatibility imposes a dependence between wall rotations. If the 2D model in Fig 4d is firstly mirrored about the  $\bar{z} = 1$  plane and then periodically repeated, the rotations of wall 1 and wall 2, at the boundary symmetry plane,  $\bar{z} = 0$  (and  $\bar{z} = 1$ ) are equal, i.e.  $\varphi_{\theta_1} = \varphi_{\theta_2}$ . This implies a dependence between the bending moments per unit length,  $M_{\theta_1}$  and  $M_{\theta_2}$ , and membrane forces per unit length,  $N_{z_1}$  and  $N_{z_2}$ , of walls 1 and 2, a situation which is expected to breakdown at the free ends of the double walls where forces normal to free surfaces vanish. Away from such regions, the governing equations for a uniform thermal gradient,  $\Delta T/t_1$ , across wall 1 (see Fig 4c), are derived based on classical beam-plate theory and by considering that equal wall rotations ( $\varphi_{\theta_1} = \varphi_{\theta_2}$ ) for small strains implies equal wall bending curvatures i.e.  $\kappa_{\theta_1} = \kappa_{\theta_2}$ , giving two kinematic and two equilibrium relations (for plane stress):

$$\left. \begin{aligned} \kappa_{\theta_1} = \kappa_{\theta_2} &\rightarrow \frac{M_{\theta_1}}{EI_1} + \frac{a\Delta T}{t_1} = \frac{M_{\theta_2}}{EI_2} \quad (i) \\ \bar{\varepsilon}_{z_1} = \bar{\varepsilon}_{z_2} + \kappa_{\theta_2}\mathcal{H} &\rightarrow \frac{N_{z_1}}{Et_1} + \frac{a\Delta T}{2} = \frac{N_{z_2}}{Et_2} + \frac{M_{\theta_2}}{EI_2}\mathcal{H} \quad (ii) \\ N_{z_1} + N_{z_2} &= 0 \quad (iii) \end{aligned} \right\} \quad (1)$$

$$M_{\theta_1} + M_{\theta_2} + N_{z_1}\mathcal{H} = 0 \quad (iv)$$

where  $E$  (MPa) is the elastic modulus,  $a$  (1/K) is the coefficient of thermal expansion,  $\bar{\varepsilon}_{z_1}$  and  $\bar{\varepsilon}_{z_2}$  are the total membrane strains at the neutral-central axes ( $\bar{y} = 0$ ) of walls 1 and 2, which are separated by a distance,  $\mathcal{H} = H + (t_1 + t_2)/2$  (Fig 1c), and  $I_1 = t_1^3/12$ ,  $I_2 = t_2^3/12$ , are the second moments of area per unit length of walls 1 and 2. The nominal stress as a function of through thickness position,  $\bar{y}$ , ( $-1 \leq \bar{y} \leq 1$ ), in wall 1 by beam theory is,  $\sigma_{z_1}(\bar{y}) = (M_{\theta_1}/I_1)(t_1/2)\bar{y} + N_{z_1}/t_1$ , which by solving Equations 1(i – iv) gives:

$$\sigma_{z_1}(\bar{y}, \hat{H}, \hat{t}_2) = (f(\hat{H}, \hat{t}_2) + \bar{y}g(\hat{H}, \hat{t}_2))Ea\Delta T \quad (2)$$

where  $f(\hat{H}, \hat{t}_2)$  and  $g(\hat{H}, \hat{t}_2)$  are monotonically increasing geometric functions of skin spacing ratio,  $\hat{H}$ , and skin thickness ratio,  $\hat{t}_2$ . A similar stress function applies in wall 2, and if axisymmetry about the  $\theta''$  axis is considered, as in Fig 4c, the stresses in Equation (2) still hold approximately, but scaled by  $(1 - \nu)$ , where  $\nu$  is Poisson's ratio [20]. In summary, Equations 1(i – iv) and (2) demonstrate that the larger the skin spacing and inner skin thickness, the higher the degree by which inner wall 2 constraints the rotation and extension of outer wall 1, and hence the higher the stresses in wall 1. Externally, however, the double wall system is so far considered unconstrained, and the net rotations (and extensions) are non-zero i.e.  $\varphi_{\theta_1} = \varphi_{\theta_2} \neq 0$ .

### 2.3.2 Externally constrained zero rotations in flat double walls

We now consider the case of externally constrained rotations e.g. through an external moment applied by a fixed or sliding boundary. This eliminates any dependence between the bending moments,  $M_{\theta_1}$ ,  $M_{\theta_2}$ , of the two walls, simplifying Equations 1(i – iv) into:

$$\left. \begin{aligned} \kappa_{\theta_1} = 0 &\rightarrow \frac{M_{\theta_1}}{EI_1} + \frac{a\Delta T}{t_1} = 0 \quad (i) \\ \kappa_{\theta_2} = 0 &\rightarrow M_{\theta_2} = 0 \quad (ii) \\ \bar{\varepsilon}_{z_1} = \bar{\varepsilon}_{z_2} &\rightarrow \frac{N_{z_1}}{Et_1} + \frac{a\Delta T}{2} = \frac{N_{z_2}}{Et_2} \quad (iii) \\ N_{z_1} + N_{z_2} &= 0 \quad (iv) \end{aligned} \right\} \quad (3)$$

and the stress solution (Equation (2)) to:

$$\sigma_{z_1}(\bar{y}, \hat{t}_2) = (h(\hat{t}_2) + \bar{y}k(\hat{t}_2))Ea\Delta T \quad (4)$$

where the geometric parameters  $h(\hat{t}_2)$  and  $k(\hat{t}_2)$  depend only on the skin thickness ratio,  $\hat{t}_2$ . Notably, in double wall systems which are flat, both internally constrained non-zero rotations (Equation (2)) and externally constrained zero rotations (Equation (4)) give theoretical nominal stress distributions which do not change with position with respect to the pedestal.

### 2.3.3 Self-constrained zero rotations in self connected 2D double walls

The problem becomes more complex for curved geometries, especially those with self-connected walls, i.e. the case of full circular rings, where rotations in each wall are self-constrained due to the absence of a free end. One such case is the gas turbine blade in Fig 1a, where the profile is highly curved near the leading edge, such that the convexity of the outer surface switches rapidly from convex (low pressure – suction side) to concave (high pressure side), and the walls are self-connected at the trailing edge. The 2D concentric coupled thin cylindrical rings/walls, represented by the model in Fig 4d, as well as the 3D concentric coupled long cylindrical thin walls, modelled by the unit cell in Fig 4b, are particular idealised cases of constant curvature,  $1/R$ , and constant thermal gradient,  $\Delta T/t_1$ , which give zero wall rotations,  $\varphi_{z1} = \varphi_{z2} = 0$ , due to the self-constraint in each wall (also discussed in Section 2.1.2). We utilise these cases to understand and work towards the general case of a gas turbine blade.

In the 2D case of Fig 4d, the  $\varphi_z$  rotations are self-constrained to be zero due to symmetry at the unit cell boundaries,  $\bar{\theta} = 0$ , and,  $\bar{\theta} = 1$  (for a constant  $\Delta T = T_{max} - T_{min}$  along  $\theta$ ). Since  $\varphi_{z1} = \varphi_{z2} = 0$ , the exact solution for externally constrained zero rotations in flat double walls (Equations 3(i – iv)) is a fairly good approximation here for nominal stresses in Fig 4d (if  $z$  components are converted into  $\theta$  and vice versa). This is true for small unit cell angles,  $\psi$ , implying small pedestal spacing,  $\hat{L}_\theta$ , and/or small curvatures i.e. large  $\hat{R}$ . The main difference here is that stresses vary with position from the pedestal ( $\theta$  direction), especially for large  $\psi$  i.e. large  $\hat{L}_\theta$  and low  $\hat{R}$  values, such that in both wall 1 ( $i = 1$ ) and wall 2 ( $i = 2$ ) the forces and moments take maximum values,  $N_{P\theta_i}$ ,  $M_{Pz_i}$ , at the pedestal ( $\bar{\theta} = 1$ ) and minimum values,  $N_{O\theta_i}$ ,  $M_{Oz_i}$ , at the symmetry plane away from the pedestal ( $\bar{\theta} = 0$ ), according to the equilibrium relations:

$$\left. \begin{aligned} N_{P\theta_i} &= N_{O\theta_i} \cos \psi & (i) \\ Q_{PR_i} &= N_{O\theta_i} \sin \psi & (ii) \\ M_{Pz_i} &= M_{Oz_i} + R_i(1 - \cos \psi) N_{O\theta_i} & (iii) \end{aligned} \right\} \quad (5)$$

where  $R_i$  is the centreline radius of wall 1 ( $i = 1$ ) and wall 2 ( $i = 2$ ), and  $Q_{PR_i}$  are the equal and opposite shear forces imposed by the pedestal to the walls. Based on Equation 5(ii), this implies that also  $N_{O\theta_1} = -N_{O\theta_2}$  (see Fig 1e), and that in contrast to flat double walls (Sections 2.3.1-2.3.2), here the pedestal also carries a purely tensile force (on top of other shear forces/bending moments), which impedes the relative radial,  $r$ , motion of the walls, especially near  $\bar{\theta} = 1$ ; this satisfies the condition of proportional membrane strains (at  $\bar{y} = 0$ ) between the two walls i.e.  $R_1 \bar{\epsilon}_{\theta_1} = R_2 \bar{\epsilon}_{\theta_2}$ . Application of the virtual work principle and classical beam theory provides a detailed solution for the 2D case of Fig 1e [20], for the entire range of pedestal spacing,  $\hat{L}_\theta$ ; errors can only arise at large curvatures i.e.  $\hat{R} < 20$ , where classical beam theory becomes invalid. The solution demonstrates that for small unit cell angles,  $\psi$ , bending moments between the two skins are nearly independent, such that only the inner skin thickness,  $\hat{t}_2$ , has a first order effect on stresses, mainly induced by the requirement for proportional wall extensions/contractions; this suggests a similar stress field as for the case of externally constrained rotations in flat walls (Section 2.3.2). The variation of stresses with position

from the pedestal, and non-linearities in the through thickness wall stress distribution due to curvature, are classified as second and third order effects, respectively, especially in the small pedestal spacing,  $\hat{L}_\theta$ , and small curvature ( $\hat{R} > 20$ ) regimes of interest here.

The above analysis of Fig 4d considers a hot temperature applied on the convex outer surface of the double rings. The problem is of the same nature when the hot temperature is applied on the concave outer surface of wall 2, with the main difference being that wall 2 now has the potential to expand and therefore translate radially towards wall 1. For a compressive membrane force,  $N_{\theta_2}$ , Equation 5(ii) now implies that the pedestal carries a purely compressive force, whereas Equation 5(iii) implies that the bending moment here increases with distance from the pedestal i.e.  $M_{O_{z_2}} > M_{P_{z_2}}$  (See Fig 1e); the difference between  $M_{O_{z_2}}$  and  $M_{P_{z_2}}$  increases with unit cell angle,  $\psi$  i.e. with increasing,  $\hat{L}_\theta$ , and/or decreasing,  $\hat{R}$ .

### 2.3.4 Self-constrained zero rotations in self-connected 3D double walls

2D phenomena for the coupled concentric walls in Fig 1e, apply in the  $\theta$  direction for the 3D coupled concentric cylindrical walls of Fig 4b, i.e.  $\varphi_{z_1} = \varphi_{z_2} = 0$ , at  $\bar{\theta} = 0$ , and  $\bar{\theta} = 1$ . Self-constraint in the longitudinal,  $z$  direction, however, is induced differently. Consider a single, long cylindrical wall with a constant thermal gradient,  $\Delta T/t_1$ , through its thickness. Away from the free ends, a potential thermal curvature,  $a\Delta T/t_1$ , of an elemental ( $d\theta$ ) long strip of the cylindrical wall, interferes with the same curvatures of adjacent strips, such that a moment,  $M_{\theta_1} = -EI_1 a\Delta T/t_1$ , is uniformly generated circumferentially, such that the net rotation is self-constrained to zero i.e.  $\varphi_{\theta_1} = 0$  (generalised plane strain); this is consistent with the results of Section 2.1.2 of the actual turbine blade configurations for both single and double walls. However, it should be noted that if  $\Delta T$  varies with  $\theta$  and/or  $z$ , then potential thermal curvatures also vary, such that  $\varphi_{\theta_1}(\theta, z) \neq 0$ . Regardless of the constancy of  $\Delta T$ , the generalised plane strain condition i.e.  $\varphi_{\theta_1} = 0$ , breaks down locally near traction-free ends where  $M_{\theta_1}$  and  $N_{z_1}$  must equal zero [52]. As a result, local non-zero  $\varphi_{\theta_1}(z)$  rotations exist (for constant  $\Delta T$ ) which can be only ‘partially’ self-constrained, in the circumferential direction, by a local membrane force  $N_{\theta_1}$ . Now, if the high temperature is applied on the outer convex surface,  $N_{\theta_1}$  is compressive as it resists contraction in the cylindrical wall imposed by the inward radial,  $r$ , deflections (see Fig 1c) associated with  $\varphi_{\theta_1}(\theta, z) \neq 0$ . In the inverse scenario of high temperature at the inner concave surface of the cylindrical wall,  $N_{\theta_1}$  becomes tensile to resist an outward local deflection of the wall. Again, all the above are consistent with the kinematic behaviour shown earlier in Figs 2a-b and Figs 2d-e near the traction-free ends (at  $z = 60$  mm) of the single and double wall blade components, where the walls generally rotate towards the interior of the blade. We specifically find that at the pressure side of the blade where the hot outer surface is concave, the tensile stresses at the inner surface of the outer wall increase locally (see Fig 2e), whereas at the suction side where the hot outer surface is convex, a local increase of compressive stresses occurs (see Fig 2e).

Deflection based solutions [52, 54] describe the local transition of the stress field for this particular problem. If a circular cap is added at the end of the cylindrical wall, then the local non-zero  $\varphi_{\theta_1}(z)$  rotations at the wall end will be also resisted by the flexural stiffness of the cap, in addition to the

force  $N_{\theta_1}$ . In summary, both free end and capped end conditions are complex cases where  $\varphi_{\theta_1}(z)$  rotations are partially self-constrained and are non-zero.

Now consider the coupling of the outer cylindrical wall with the inner wall. When  $\Delta T$  varies throughout the outer wall and/or at free or capped ends of the system, the condition,  $\varphi_{\theta_1}(z) \neq 0$ , applies. Thus, some features of the idealised general case of internally constrained non-zero rotations (Section 2.3.1) are expected to arise, such as a dependence between wall bending moments,  $M_{\theta_1}$  and  $M_{\theta_2}$ , and the associated role of wall spacing,  $\hat{H}$ . For example, Fig 2a-b clearly shows that the presence of the inner wall limits the net rotation of the coupled walls towards the interior of the blade, locally at the traction-free end, compared to the much larger local rotations of the single wall in Figs 2d-e; also note that the deformation scaling factor in Figs 2d-e is 1/2 of the factor used in Figs 2a-b. However, for a constant  $\Delta T$  profile and away from the ends of a double wall cylindrical system, the condition,  $\varphi_{\theta_1} = \varphi_{\theta_2} = 0$ , prevails (along with  $\varphi_{z_1} = \varphi_{z_2} = 0$ ), such that  $M_{\theta_1}$  and  $M_{\theta_2}$  are independent and the system of Equations 3(i – iv) is relevant. In this case, wall coupling along the  $z$  direction (Fig 1c) only enforces a common extension/contraction. This is consistent with the response away from the ends of the double wall turbine blade shown earlier in Figs 2a-c, in which the rotations are also mainly constrained to zero, and the walls are found to exhibit common extension along the axial,  $z$ , direction of the blade.

### 2.3.5 Combined constraints – practical aspects

In reality, for the 3D self-connected double wall blade systems (Fig 1a), the rotation of each wall will be self-constrained differently in the two principal directions,  $\theta$  and  $z$ , and rotations will be generally non-zero. This is expected mainly due to the typical variation of thermal gradient,  $\Delta T/t_1$ , throughout the outer wall as well as a typical variation of the wall thickness profile [1, 28]. The significance of these variations for the thermal stress field will be covered in a future study. Here we consider the following two idealised relevant cases, *A* and *B* (for  $\Delta T$  and  $\hat{R}$  constant).

- A. Self-constrained zero wall rotations in both  $\theta$  and  $z$  directions i.e.  $\varphi_{z_1} = \varphi_{z_2} = \varphi_{\theta_1} = \varphi_{\theta_2} = 0$
- B. Self-constrained zero wall rotations in the  $\theta$  direction i.e.  $\varphi_{z_1} = \varphi_{z_2} = 0$ , combined with internally constrained non-zero wall rotations in the  $z$  direction, i.e.  $\varphi_{\theta_1} = \varphi_{\theta_2} \neq 0$ .

Case A is considered more important here, as zero rotations in both directions imply higher stress magnitudes and because this case resembles the stress field that occurs away from the ends of an actual gas turbine blade (Section 2.1.2). Furthermore, away from the traction-free end, additional inertial stresses and aerodynamic bending stresses (gas bending) are superimposed in practise [25, 49]. For this more critical case of combined constraints ( $\varphi_{z_1} = \varphi_{z_2} = \varphi_{\theta_1} = \varphi_{\theta_2} = 0$ ), we present an analytical 3D approximate solution, by combining the case of 2D coupled concentric rings (Section 2.3.3) for zero pedestal spacing ( $\hat{L}_\theta \rightarrow 0$ ) and small curvatures i.e.  $\hat{R} < 20$  (when classical plate theory is valid), and the generalised plane strain condition for long, coupled concentric cylindrical walls (Section 2.3.4). Specifically, by applying the system of Equations 3(i – iv) in  $\theta$  and  $r$  directions and by using superposition, we obtain:



$$\begin{aligned}
\kappa_{\theta_1} = 0 &\rightarrow \frac{M_{\theta_1}}{EI_1} - \nu \frac{M_{z_1}}{EI_1} + \frac{a\Delta T}{t_1} = 0 \quad (i) \\
\kappa_{z_1} = 0 &\rightarrow \frac{M_{z_1}}{EI_1} - \nu \frac{M_{\theta_1}}{EI_1} + \frac{a\Delta T}{t_1} = 0 \quad (ii) \\
\kappa_{\theta_2} = 0 &\rightarrow \frac{M_{\theta_2}}{EI_2} - \nu \frac{M_{z_2}}{EI_2} = 0 \quad (iii) \\
\kappa_{z_2} = 0 &\rightarrow \frac{M_{z_2}}{EI_2} - \nu \frac{M_{\theta_2}}{EI_2} = 0 \quad (iv) \\
\bar{\varepsilon}_{z_1} = \bar{\varepsilon}_{z_2} &\rightarrow \frac{\mathcal{N}_{z_1}}{Et_1s_1} - \nu \frac{N_{\theta_1}}{Et_1} + \frac{a\Delta T}{2} = \frac{\mathcal{N}_{z_2}}{Et_2s_2} - \nu \frac{N_{\theta_2}}{Et_2} \quad (v) \\
R_1\bar{\varepsilon}_{\theta_1} = \bar{\varepsilon}_{\theta_2}R_2 &\rightarrow \frac{N_{\theta_1}}{Et_1} - \nu \frac{\mathcal{N}_{z_1}}{Et_1s_1} + \frac{a\Delta T}{2} = \left( \frac{N_{\theta_2}}{Et_2} - \nu \frac{\mathcal{N}_{z_2}}{Et_2s_2} \right) \frac{R_2}{R_1} \quad (vi) \\
\mathcal{N}_{z_1} + \mathcal{N}_{z_2} &= 0 \quad (vii) \\
N_{\theta_1} + N_{\theta_2} &= 0 \quad (viii)
\end{aligned} \tag{6}$$

leading to the following first order approximation of the nominal stresses in the critical outer wall 1:

$$\begin{aligned}
\sigma_{\theta_1}(\bar{y}, \hat{t}_2, R_2/R_1) &= (m_{\theta}(\hat{t}_2, R_2/R_1) + \bar{y}w_{\theta}(\hat{t}_2, R_2/R_1))Ea\Delta T \quad (i) \\
\sigma_{z_1}(\bar{y}, \hat{t}_2, R_2/R_1) &= (m_z(\hat{t}_2, R_2/R_1) + \bar{y}w_z(\hat{t}_2, R_2/R_1))Ea\Delta T \quad (ii)
\end{aligned} \tag{7}$$

where  $\bar{y}$  is the normalised position in the wall with respect to the centre-line and  $m_{\theta,z}(\hat{t}_2, R_2/R_1)$  and  $w_{\theta,z}(\hat{t}_2, R_2/R_1)$  are geometric parameters which increase primarily with skin thickness ratio,  $\hat{t}_2$ , in both  $\theta$  and  $z$  directions, and less significantly with the ratio of wall centreline radii,  $R_2/R_1$ ; the latter is a function of skin spacing,  $H$ , and,  $\hat{t}_2$  (see Fig 4b). Note that all the bending moments (and second moment of areas) in Eqs (8), along with the membrane forces,  $N_{\theta_1}$ ,  $N_{\theta_2}$ , are per unit length, whereas the  $\mathcal{N}_{z_1}$  and  $\mathcal{N}_{z_2}$  are total membrane forces per unit cell. For  $\hat{t}_2 = R_2/R_1 = 1$ , Fig 3 demonstrates a close agreement between the approximate solution (Equation 7) and the compressive/tensile FE thermal stresses generated in the characteristic locations 1, 3, 4, 5 of the outer wall of the double wall turbine blade component of Fig 2c. A similar solution can be obtained for the less critical inner wall 2, which, based on our idealisation, experiences pure tension, i.e.  $M_{\theta_2} = M_{z_2} = 0$  (Equations 6(iii – iv)); the latter agrees with the tensile stress contours in the inner wall of Fig 2c for the double wall turbine blade system.

Equations 6(iii – iv) imply that the presence of the inner wall 2 affects only membrane forces in the system and that bending stresses in wall 1 always exist, they are equal in  $\theta$  and  $z$  directions,

and scale with  $Ea\Delta T/(1 - \nu)$ . The extreme case of  $\hat{t}_2 \rightarrow 0$  implies perfect compliance of wall 2 to the thermal extensions of wall 1, such that membrane forces are negligible for wall 1 (but not for wall 2); thus, Equations (7) converge to the solution for a single cylindrical thin wall with a uniform thermal gradient,  $\Delta T/t_1$ ,  $\sigma_{z_1} = \sigma_{\theta_1} = \pm(1/2)Ea\Delta T/(1 - \nu)$ , for  $\bar{y} = \pm 1$  (solution also plotted in Fig 3). The opposite extreme case of  $\hat{t}_2 \rightarrow \infty$  corresponds to a perfectly rigid response, where no extensions are allowed in the system due to the infinite size of wall 2 (together with zero rotations), for which the generated membrane forces are also negligible; here, Equations (7) converge to the case of a single cylindrical thin wall with fixed edges,  $\sigma_{z_1} = \sigma_{\theta_1} = \pm Ea\Delta T/(1 - \nu)$ , for  $\bar{y} = \pm 1$ .

For typical geometric ratios,  $\hat{R} = 20$ ,  $t_1 = \hat{t}_2 = \hat{H} = 1$ , which gives,  $R_2/R_1 = 0.9$  (see Fig 1c), Equation 7 give stress ratios,  $\sigma_{\theta_1}/\sigma_{z_1} \approx 0.97$  and  $\sigma_{\theta_1}/\sigma_{z_1} \approx 0.99$ , at the inner ( $\bar{y} = -1$ ) and outer ( $\bar{y} = 1$ ) surfaces of wall 1, respectively. This implies a nearly equibiaxial stress field ( $M_{\theta_1} \approx M_{z_1}$ ,  $N_{\theta_1} \approx N_{z_1}$ ); the extreme case,  $R_2/R_1 \rightarrow 1$ , corresponds to  $\sigma_{\theta_1}/\sigma_{z_1} \rightarrow 1$ .

For systems with large curvatures i.e.  $\hat{R} < 20$ , which can be considered relevant to the leading edge region of the aerofoil in Fig 1a, the role of  $R_2/R_1$  becomes important and Equation 7 yields a general biaxial stress field. At  $\hat{R} < 20$ , the validity of Equations 6(i – viii) based on classical plate theory breaks down and additional phenomena arise, such as non-linear elastic stress distributions through the wall thicknesses. For this regime, we previously derived an exact solution for coupled 2D rings, based on Airy’s stress function [20]. Although this solution can be extended in 3D space, here we analyse thin walled systems i.e.  $\hat{R} > 20$ , with large  $\hat{R}/\hat{H}$  ratios, where the effect of  $R_2/R_1$  is insignificant. Our first order 3D analytical solution (Equation (7)) is used to provide an indication of how nominal stresses scale with the primary geometric ratios,  $\hat{t}_2$ , and  $R_2/R_1$  in long coupled cylindrical walls. For this practical range of parameters, higher order 3D analytical solutions that account for the variation of stresses with respect to the pedestal, such as our 2D detailed solution for coupled rings [20], are not judged necessary. Such 3D effects are studied using 3D FE analysis.

## 2.4 FE modelling – implementation of constraints

The FE simulations of the 3D unit cell model in Fig 4b involve the same type of temperature-displacement numerical analysis and elements, as well as the same material model parameters as those described for the 3D turbine blade models in Section 2.1.1. For the 2D models in Figs 4c-d, we use plane stress elements. For the 3D model of Fig 4b, at all the nodes at the symmetry boundary planes  $\bar{\theta} = 0$  and  $\bar{\theta} = 1$  we apply  $u_\theta = 0$  ( $u$ -refers to displacements), whereas for nodes at the symmetry plane  $\bar{z} = 1$  we enforce  $u_z = 0$  (consider a  $r\theta z$  system with origin at the centre of curvature  $1/R$  and note that 3D solid elements do not possess rotational degrees of freedom (DOFs)). Therefore, in the FE implementation, case A ( $\varphi_{z_1} = \varphi_{z_2} = \varphi_{\theta_1} = \varphi_{\theta_2} = 0$ ) and case B ( $\varphi_{z_1} = \varphi_{z_2} = 0$  and  $\varphi_{\theta_1} = \varphi_{\theta_2} \neq 0$ ) described in Section 2.3.5, differ only in terms of the condition for wall rotations about  $\theta$  at the symmetry plane,  $\bar{z} = 0$  (purple faces in Fig 4b).

For case A (zero  $\theta$  wall rotations), we enforce all nodes at  $\bar{z} = 0$  (dependent nodes) to have the same  $u_z$  as a reference node,  $\mathcal{S}$  (independent node), while nodes at the intersections of  $\bar{z} = 0$  with the planes  $\bar{\theta} = 0$  and  $\bar{\theta} = 1$ , are additionally set to have the same  $u_\theta$  as  $\mathcal{S}$ ; the latter is then set to satisfy  $u_\theta = \varphi_\theta = 0$ .

For case B (non-zero  $\theta$  wall rotations) the constraint is more complex. We consider that the unit cell in Fig 4b is circularly repeated along  $\theta$ , such that the non-zero  $\varphi_\theta$  rotations at the boundary/symmetry plane,  $\bar{z} = 0$ , occur in an axisymmetric manner about the principal  $z$  axis of the

cylindrical geometry. This implies that plane,  $\bar{z} = 0$ , becomes conical and has a vertex ( $r = 0$ ) that translates only along the  $z$  axis. This implies that any boundary node on plane,  $\bar{z} = 0$ , will always satisfy the equation,  $r = c_1 z + c_2$  ( $r\theta z$  system), where  $r\theta z$  are the original or current nodal coordinates and  $c_1, c_2$ , are unknown constants that define the conical plane. Any set of current coordinates,  $r_1, z_1, r_2, z_2$ , of two nodes, 1 and 2, that belong to the initial plane,  $\bar{z} = 0$  (see Fig 4b), must satisfy the above form, and thus defines the constants  $c_1 = (r_1 - r_2)/(z_1 - z_2)$  and  $c_2 = r_2 - c_1 z_2$ . This does not yet fully define a surface axisymmetric about the  $z$  axis, in 3D space, and an additional node is required. Any additional node,  $i$ , in the plane  $\bar{z} = 0$  (Fig 4b), is considered dependent as it must comply with  $r_i = c_1 z_i + c_2$  for the constants  $c_1$  and  $c_2$  defined by the ‘independent’ nodes, 1 and 2. This fully defines the surface in terms of six current coordinates as:

$$(r_1 - r_2)(z_1 - z_i) + (z_2 - z_1)(r_1 - r_i) = 0 \quad (8)$$

For each FE analysis iteration, we demand that Equation (8) is satisfied for all the remaining dependent nodes,  $i$ , in the plane  $\bar{z} = 0$  (Fig 4b), while keeping the same independent nodes, 1 and 2. Each current nodal coordinate is the sum of current nodal displacement and original coordinate, such that the numerical task of the FE solver for each thermal loading increment here, is to determine the displacement increments that simultaneously satisfy a total of  $n - 2$  equations with the form of Equation (8), for a total of  $n$  nodes in  $\bar{z} = 0$  plane.

We implement the above framework within the ABAQUS Multi-Point Constraint (MPC) subroutine. Further details on the required displacement derivatives underpinning Equation (8), are provided in the Appendix.

## 3 Results and discussion

### 3.1 Nature of 2D stress field

Fig 5 compares maximum absolute principal stresses,  $\sigma = \max(|\sigma_1|, |\sigma_2|, |\sigma_3|)$ , normalised with respect to the thermal loading factor,  $E\alpha\Delta T$ , for four characteristic structural constraint scenarios in 2D space. Geometry is fixed, with ratios:  $\hat{L}_{z,\theta} = \hat{t}_2 = \hat{H} = \hat{D}_p = 1$ , and  $\hat{\rho}_{Pf} = 0.1$ ; for the double rings in Figs 5c-d, a radius of curvature,  $\hat{R} = 20$ , is also used. Fig 5a (FE model in Fig 4c) is consistent with Section 2.3.1, in that the thermal rotation of wall 1 is constrained internally by wall 2, such that bending moments and axial forces are generated in both walls; bending dominates over membrane forces i.e. the stress distribution is nearly symmetric in both walls (see Fig 5(a)). On the other hand, Fig 5b (FE model in Fig 4d) agrees with Section 2.3.2, where the thermal rotation of wall 1 is constrained externally, such that only its thermal extension is constrained internally; the latter implies that wall 2 in Fig 5b experiences only a tensile membrane force. Furthermore, the wall extensions must be equal in Fig 2b, resulting in much larger membrane forces compared to the case of Fig 5a, where extensions must be proportional. As a consequence, the important feature here is that a large compressive force in wall 1 acts to reduce tensile stresses at its inner edge and increase compressive stresses at its outer edge (see Fig 5b). The same occurs in the double ring geometries in Figs 5c-c’, with the only difference that rotations are self-constrained by the geometry itself. This verifies our statement in Section 2.3.1 that compatible wall extensions are primarily responsible for stresses in both the case of externally constrained rotations in flat double walls and the case of self-

constrained rotations in self-connected walls/rings. Figs 5c-c' also agree with the analysis of Section 2.3.3, on the basis that for the small unit cell angles,  $\psi$ , studied here, i.e. small pedestal spacing,  $\hat{L}_\theta = 2$ , combined with large radius of curvature,  $\hat{R} = 20$ , the stress variation with position,  $\theta$ , from the pedestal is small; this occurs both when a hot temperature is applied at the external convex surface/edge or at the internal concave edge of the concentric double rings. All the above observations confirm our theoretical analysis of structural constraints-geometries in 2D space (Sections 2.3.1-2.3.3), based on which we now evaluate the 3D FE results.

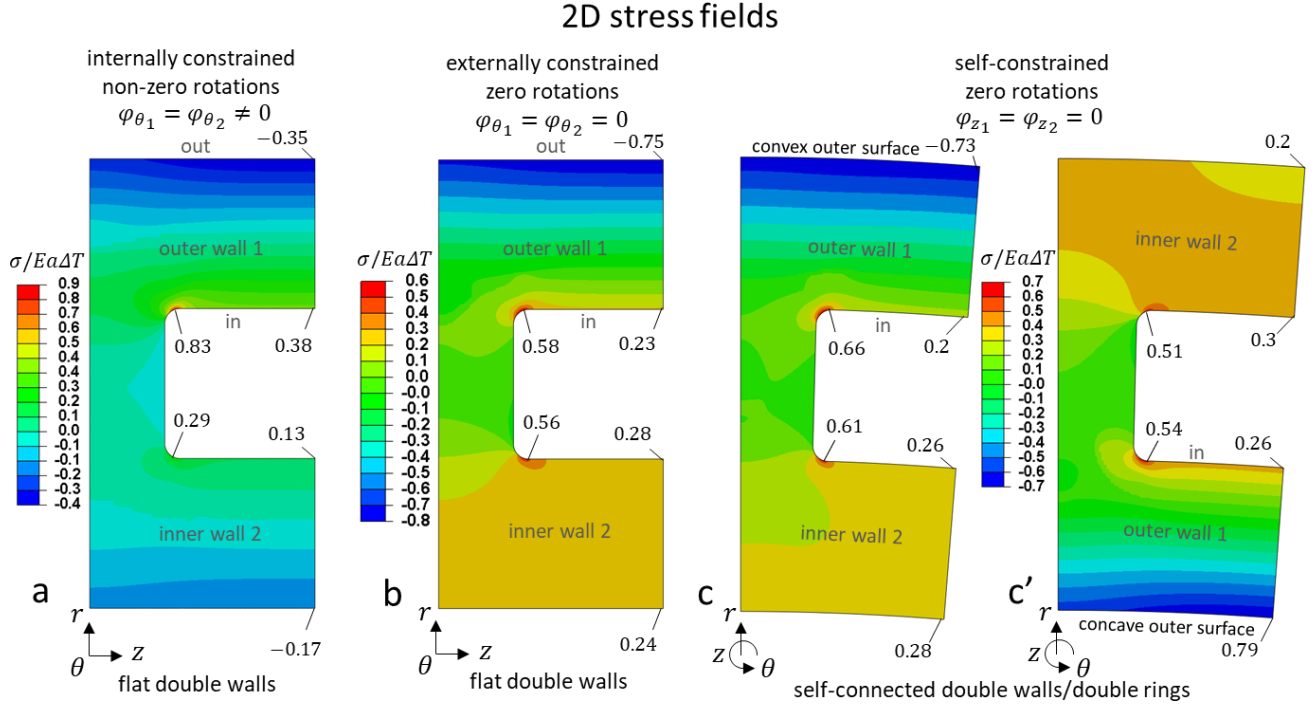


Figure 5. Comparison of 2D FE thermal stress fields between four double wall scenarios; contours show maximum absolute principal stress normalised with respect to  $E\alpha\Delta T$ . Geometric ratios (Section 2.2) include:  $\hat{R} = 20$ ,  $\hat{L}_z = \hat{L}_\theta = 2$ ,  $\hat{t}_2 = \hat{H} = \hat{D}_p = 1$ , and  $\hat{\rho}_{pf} = 0.1$ . Cases correspond to: (a) internally constrained rotations ( $\varphi_{\theta_1} = \varphi_{\theta_2} \neq 0$ ) in flat double walls, (b) externally constrained zero rotations ( $\varphi_{\theta_1} = \varphi_{\theta_2} = 0$ ) in flat double walls, (c) self-constrained zero rotations ( $\varphi_{z_1} = \varphi_{z_2} = 0$ ) in double rings with a high temperature applied on the convex outer surface, and, (c') self-constrained zero rotations in double rings with the hot temperature on the concave outer surface (note: for this case the reference to walls 1, 2 is inverted).

### 3.2 Nature of 3D stress field

Stresses in the  $\theta$ ,  $z$ ,  $r$ , directions and maximum absolute principal stresses,  $\sigma = \max(|\sigma_1|, |\sigma_2|, |\sigma_3|)$ , for constraint case A ( $\varphi_{z_1} = \varphi_{z_2} = \varphi_{\theta_1} = \varphi_{\theta_2} = 0$ ) and case B ( $\varphi_{z_1} = \varphi_{z_2} = 0$  and  $\varphi_{\theta_1} = \varphi_{\theta_2} \neq 0$ ) are shown in Fig 6a-d and Fig 6a'-d', respectively. The geometry studied corresponds to ratios,  $\hat{R} = 20$ ,  $\hat{L}_{z,\theta} = 2$ ,  $\hat{t}_2 = \hat{H} = \hat{D}_p = 1$  and  $\hat{\rho}_{pf} = 0.1$  (denoted in Fig 4b). In both cases A-B, radial (tensile) stresses,  $\sigma_r$ , only exist through the pedestal (see Figs 6c, 6c'), resulting in local triaxial stress states at the pedestal fillets and biaxial stress states throughout the walls, away from the fillets. The maximum absolute principal stress,  $\sigma$ , contours (Figs 6d, 6d') can be interpreted mainly based on the circumferential stress,  $\sigma_\theta$ , (Figs 6a, 6a') and longitudinal stress,  $\sigma_z$ , (Figs 6b, 6b') distributions.

For case A (zero rotations in both directions), the  $\sigma_\theta$  (Fig 6a) and  $\sigma_z$  (Fig 6b) fields are nearly identical, and of the same nature as the 2D field for externally constrained zero rotations in Fig 5b i.e. wall 2 in pure tension as well as large compressive stresses in the outer surface of wall 1 compared to tensile stresses in the inner surface of wall 1. It is also worth noting that the principal stress,  $\sigma$ , contours in Fig 6d are very similar to the corresponding contours shown in Fig 2c for the double wall turbine blade system, adding credibility to our unit cell idealisations. On the other hand, when rotations are non-zero (and equal) about the  $\theta$  direction i.e. case B, the  $\sigma_\theta$  and  $\sigma_z$  distributions are different. Specifically,  $\sigma_z$  stresses (Fig 6b') are distributed in the same manner as the 2D case of internally constrained, non-zero rotations in Fig 5a, i.e. significant bending in both walls and small membrane forces, whereas the  $\sigma_\theta$  distribution (Fig 6a') mainly shows features of the 2D case of externally constrained zero rotations (Fig 5b). The above discussion demonstrates that the 2D analyses in the  $r - z$  and  $r - \theta$  planes replicate the  $\sigma_z$  and  $\sigma_\theta$  stress distributions, respectively, observed in the more realistic 3D unit cell. Thus, the 2D analyses capture the main characteristics of the 3D thermal stress field.

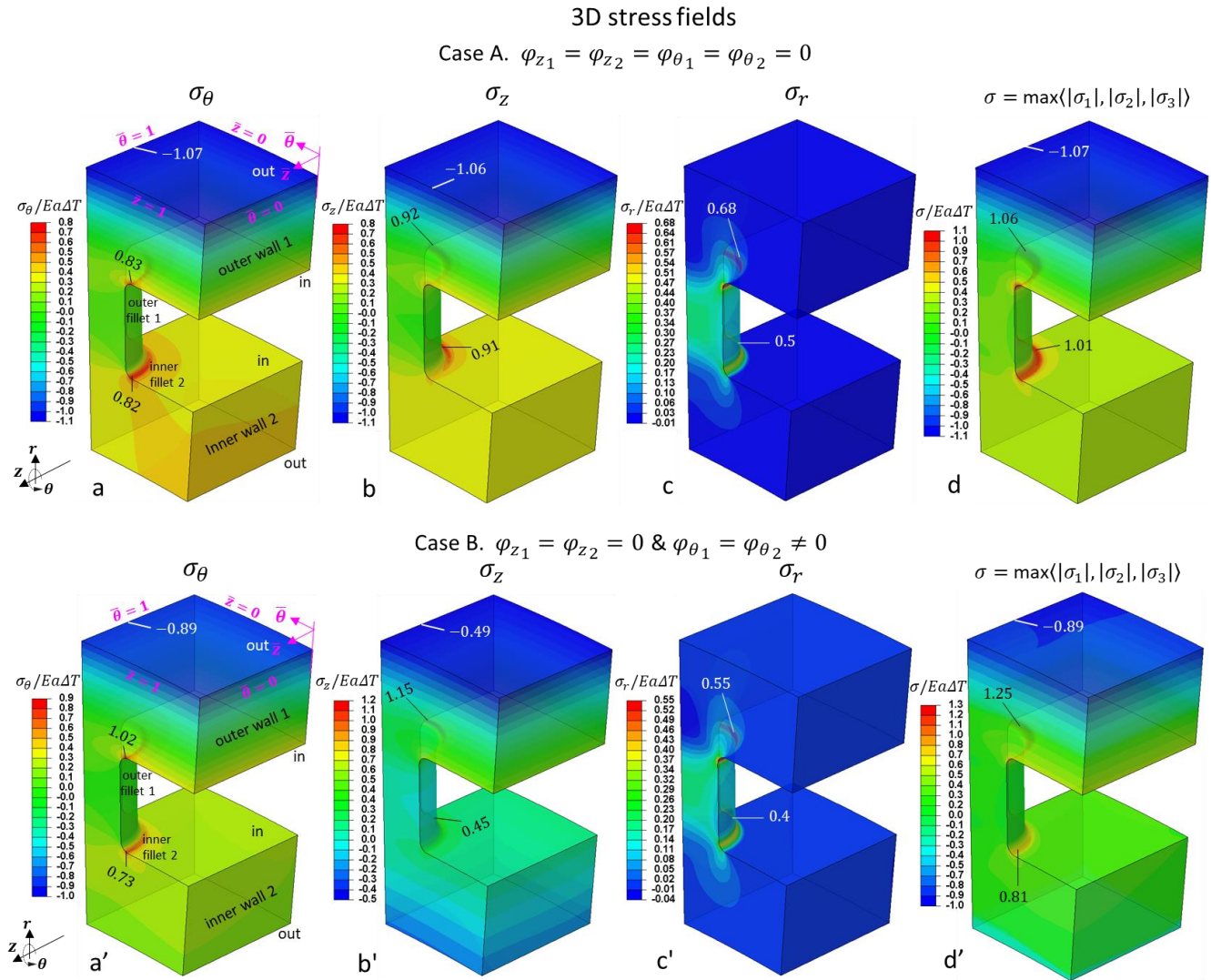


Figure 6. Comparison of 3D FE thermal stress fields for constraint cases A-B for the unit cell in Fig 4b. Geometric ratios (Section 2.2) include:  $\hat{R} = 20$ ,  $\hat{L}_{\theta,z} = 2$ ,  $\hat{t}_2 = \hat{H} = \hat{D}_p = 1$ , and  $\hat{\rho}_{Pf} = 0.1$ . For case A ( $\varphi_{z1} = \varphi_{z2} = \varphi_{\theta1} = \varphi_{\theta2} = 0$ ) FE contours represent: (a) circumferential stresses,  $\sigma_\theta$ , (b) longitudinal stresses,  $\sigma_z$ , (c) radial stresses,  $\sigma_r$ , and, (d) maximum absolute principal stresses,  $\sigma$ ; all stresses are normalised with respect to  $Ea\Delta T$ . In the same order, contours a'-d' show stresses for case B ( $\varphi_{z1} = \varphi_{z2} = 0$  &  $\varphi_{\theta1} = \varphi_{\theta2} \neq 0$ ). Critical compressive and tensile stresses are indicated in the figures.

The primary differences in the 3D stresses between constraint cases A-B, is illustrated in Figs 7. In particular, Figs 7a-b show that regardless of pedestal spacing,  $\hat{L}_{\theta,z}$ , constraining all the wall rotations to zero i.e. case A, increases the compressive stresses at all boundary points/corners of the outer surface of wall 1, and decreases tensile stresses throughout the inner surface of wall 1. This is because, as shown in 2D space (Section 3.1), and also here in 3D for case A, the kinematic condition of equal wall extensions in the  $z$  direction results in markedly larger compressive membrane forces,  $N_{z1}(= -N_{z2})$ , in wall 1, compared to case B. The fact that similar conditions also apply in case A in the  $\theta$  direction (due to  $\varphi_{z1} = \varphi_{z2} = \varphi_{\theta1} = \varphi_{\theta2} = 0$ ) results in stress ratios that fluctuate around  $\sigma_z/\sigma_\theta = 1$ , i.e. equibiaxial stress states, throughout the outer wall 1. Instead, the very low membrane forces in the  $z$  direction for case B (compared to bending moments), underpin the main trend of Fig 4d, in that throughout the tensile inner surface of wall 1,  $\sigma_z$  components are larger than  $\sigma_\theta$ , while the opposite occurs in the compressive outer surface of wall 1. Therefore, away from pedestal fillets, case B involves biaxial stress states, as well as a change in the direction of the maximum principal stress between the inner and outer surface of wall 1.

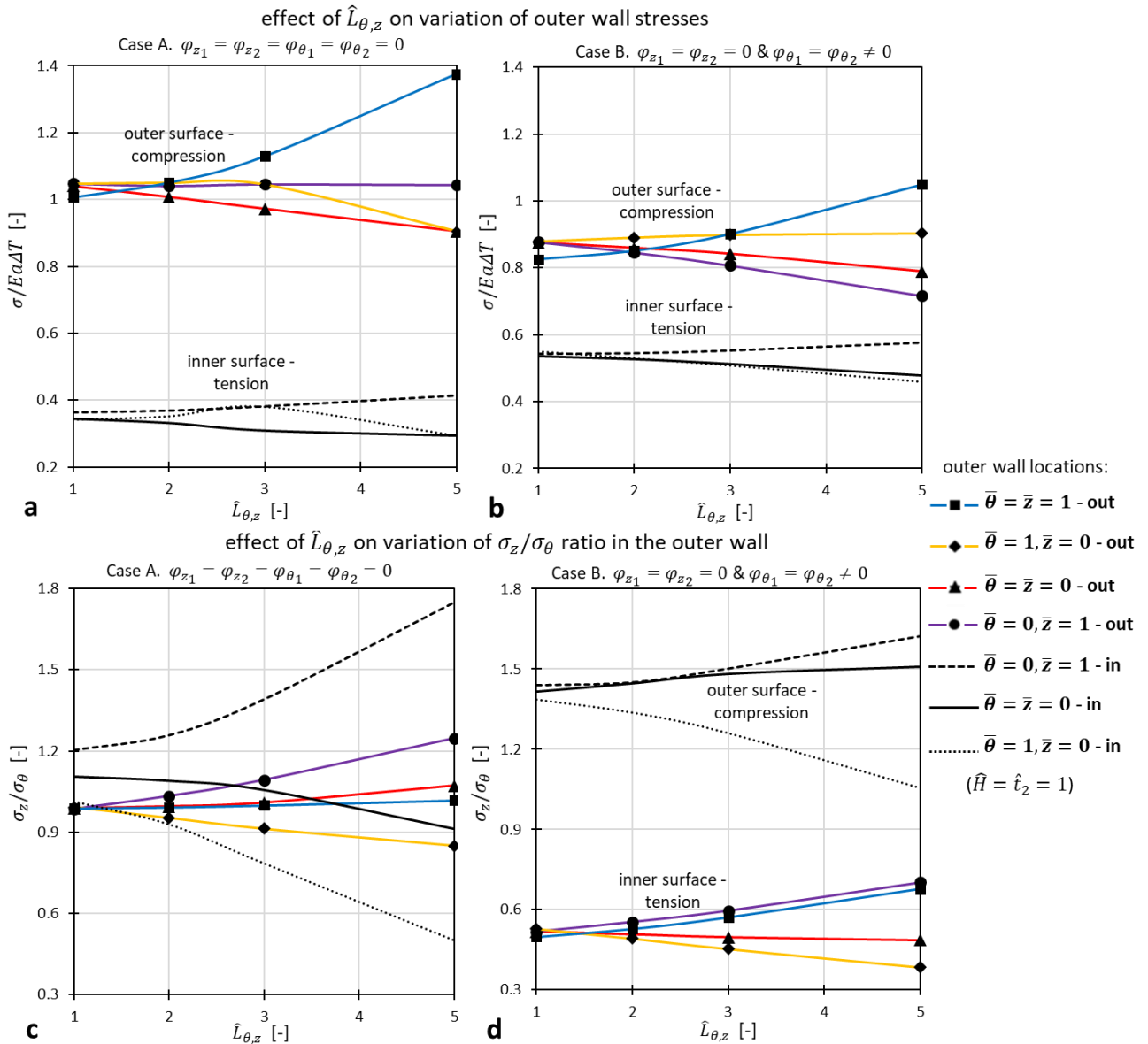


Figure 7. Variation of stress states at characteristic surface points throughout the double wall system of Fig 4b for constraint cases A-B. Plots show: (a-b) effect of pedestal spacing,  $\hat{L}_{\theta,z}$ , on compressive and tensile stresses,  $\sigma$ , at various locations of the outer wall 1, for cases A-B, and, (c-d) effect of pedestal spacing,  $\hat{L}_{\theta,z}$ , on the stress ratio,  $\sigma_z/\sigma_\theta$ , at the same outer wall 1 locations for cases A-B. Fixed geometric ratios (Section 2.1) include:  $\hat{R} = 20$ ,  $\hat{t}_2 = \hat{H} = \hat{D}_p = 1$  and  $\hat{\rho}_{Pf} = 0.1$ .



A higher order characteristic in Fig 7 is the variation of wall 1 stresses,  $\sigma$  (Figs 7a-b), and stress ratios,  $\sigma_z/\sigma_\theta$  (Figs 7c-d), with position from the pedestal. In both cases A-B, these variations become increasingly sensitive to pedestal spacing,  $\hat{L}_{z,\theta}$ . For example,  $\sigma$  stress variation in Figs 6d, 3d' is almost non-existent due to  $\hat{L}_{z,\theta} = 2$ , whereas for  $\hat{L}_{z,\theta} = 5$  in Figs 8a-b the variation in the compressive stresses of the outer surface of wall 1 is more significant; note that a deformation scale factor of 50 is used in Figs 8a-b to also illustrate the difference in structural kinematics between the constraint cases A-B. The important feature associated with this variation, is that in both Figs 7a-b the compressive stresses at the outer surface of wall 1 are higher above the pedestal ( $\bar{\theta} = \bar{z} = 1$  - out) and lower at any other location away from the pedestal, at large pedestal spacing i.e.  $\hat{L}_{z,\theta} > 3$ . The variation of the stress ratio,  $\sigma_z/\sigma_\theta$ , in Figs 7c-d is rather complex to interpret. Generally, Figs 8a-b show that except for the locations:  $\bar{\theta} = \bar{z} = 1$  - outer, and,  $\bar{\theta} = 0, \bar{z} = 1$  - inner, at all the other boundary points/corners of the unit cell in the outer wall, away from pedestal, the compressive and tensile stresses decrease with pedestal spacing,  $\hat{L}_{z,\theta}$ . Again, this is consistent with our 2D analysis of coupled cylindrical walls/rings described in Section 2.3.3, adding further significance to 2D considerations for the analysis and design of double wall systems. However, Figs 8a-b also indicate that 3D analysis is essential in capturing differences in stress magnitudes and principal stress ratios between various unit cell locations, including how these values are modified with  $\hat{L}_{z,\theta}$ .

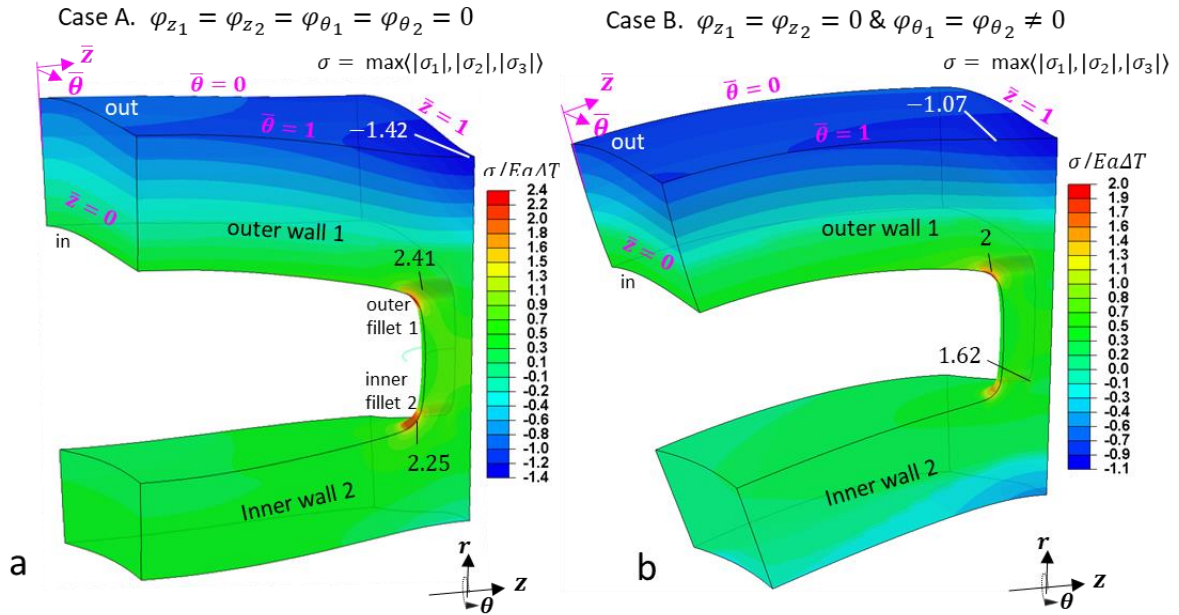


Figure 8. Comparison of 3D FE thermal stresses,  $\sigma$ , and structural kinematic response for constraint case A (a) and case B (b) for the unit cell in Fig 4b with large pedestal spacing,  $\hat{L}_{\theta,z} = 5$ . Other geometric ratios (Section 2.2) include:  $\hat{R} = 20$ ,  $\hat{t}_2 = \hat{H} = \hat{D}_p = 1$ , and  $\hat{\rho}_{pf} = 0.1$ . Critical compressive and tensile stresses are indicated in the figures.

This information can be useful in identifying suitable locations for the effusion holes, on the basis that actual peak stresses in the presence of holes have been found largely dependent on the corresponding nominal stresses (in the absence of holes) [20]. In addition, knowledge of how the principal stress ratio parameter,  $\sigma_z/\sigma_\theta$ , is distributed throughout wall 1 is important because the ratio  $\sigma_z/\sigma_\theta$  influences the degree of stress concentration around a hole. The above also apply to impingement hole stresses; these, however, are deemed far less critical for failure. For this reason, we focus here on stresses in the outer wall 1, where the effusion hole exists. In design, emphasis is



generally given to the small pedestal spacing regime,  $\hat{L}_{z,\theta} < 3$ , as the latter has been shown to improve the overall cooling performance of the system. For  $\hat{L}_{z,\theta} < 3$  the variation in stresses (and stress ratios) is rather weak (see Figs 7a-b), and therefore we will study geometry-stress relationships for a single, outer wall 1 location,  $\bar{\theta} = \bar{z} = 0$ , as the representative effusion hole location, as well as for the pedestal fillets.

### 3.3 Role of primary geometric features

#### 3.3.1 Combined effect of wall thickness and pedestal spacing

The combined effect of inner wall thickness,  $\hat{t}_2$ , and pedestal spacing,  $\hat{L}_{z,\theta}$ , on outer wall 1 stresses at  $\bar{\theta} = \bar{z} = 0$ , is plotted in Figs 9a-b, for cases A-B; in the same manner, the effect on outer and inner pedestal fillet stresses is plotted in Figs 9c-d. Fixed geometric ratios include:  $\hat{R} = 20$ ,  $\hat{H} = \hat{D}_p = 1$  and  $\hat{p}_{pf} = 0.1$ . Generally, in both cases, pedestal spacing,  $\hat{L}_{z,\theta}$ , increases pedestal stresses (see Figs 9c-d), and decreases wall 1 stresses away from the pedestals (see Figs 9a-b); both effects are more pronounced at large  $\hat{t}_2$ . For case A, Fig 9a also shows that as  $\hat{L}_{z,\theta}$  is decreased, the FE results progressively approach our approximate analytical solution (Equation (7) in Section 2.3.5) that assumes no variation with position,  $\bar{\theta}, \bar{z}$ , from the pedestal i.e.  $\hat{L}_{z,\theta} \rightarrow 0$ .

The analytical solution captures well the effect of inner skin thickness in Fig 9a for case A, in that increasing  $\hat{t}_2$ , increases compressive and decreases tensile stresses in the outer and inner surfaces of wall 1, respectively. This role of  $\hat{t}_2$  is consistent with our theoretical 2D solution in Section 2.3.2, which indicates that increasing,  $\hat{t}_2$ , enhances the compressive membrane force,  $N_{z1} (= -N_{z2})$ , in wall 1, eventually increasing the outer surface compressive stresses and decreasing the inner surface tensile stresses. Although the same applies for the compressive stresses in case B (see Fig 9b), the tensile stresses are less sensitive to  $\hat{t}_2$ . Again, this is explained by the 2D analysis in Section 2.3.1, which indicates that the condition,  $\varphi_{\theta 1} = \varphi_{\theta 2} \neq 0$ , implies that increasing  $\hat{t}_2$  not only leads to increasingly compressive membrane forces,  $N_{z1}$ , but simultaneously enhances the bending moment,  $M_{\theta 1}$ , in the outer wall 1.

The presence of these two effects associated with the condition,  $\varphi_{\theta 1} = \varphi_{\theta 2} \neq 0$ , generally leads to more complex trends for case B compared to case A, regarding the critical tensile stresses in the system, especially the tensile pedestal stresses (Figs 9c-d). This is because these stresses scale with the nominal wall stresses at the corresponding pedestal fillet locations, multiplied by a Stress Concentration Factor (*SCF*). On this basis, we can deduce that the stresses in the outer pedestal fillet in Fig 9d (case B) initially reduce with increasing  $\hat{t}_2$  for  $\hat{t}_2 \leq 0.5$ , because in this regime the effect of  $N_{z1}$  on the (nominal) tensile stresses at the inner surface of wall 1 is more dominant than the effect of  $M_{\theta 1}$ ; for  $\hat{t}_2 > 0.5$ , however, the effect of increasing  $M_{\theta 1}$  with  $\hat{t}_2$  is more dominant, such that the pedestal outer fillet stresses increase with increasing  $\hat{t}_2$ ; similar competing effects are found to apply for the stress at the inner pedestal fillet for case B (Fig 9d). The main trend in Fig 9d (case B), is that for the regime of interest,  $\hat{L}_{z,\theta} < 3$ , stresses in the outer pedestal fillet are more critical than inner fillet stresses, even at low  $\hat{t}_2$  values. In case A, however, tension in the inner wall 2 is more severe (compare Figs 6a-b with Figs 6a'-b'), such that decreasing  $\hat{t}_2$  can lead to higher stresses in the inner pedestal fillet than in the outer pedestal fillet (see Fig 9c). Nevertheless, for  $\hat{L}_{z,\theta} < 3$  the level of stress in both fillets mainly decreases with decreasing  $\hat{t}_2$ .

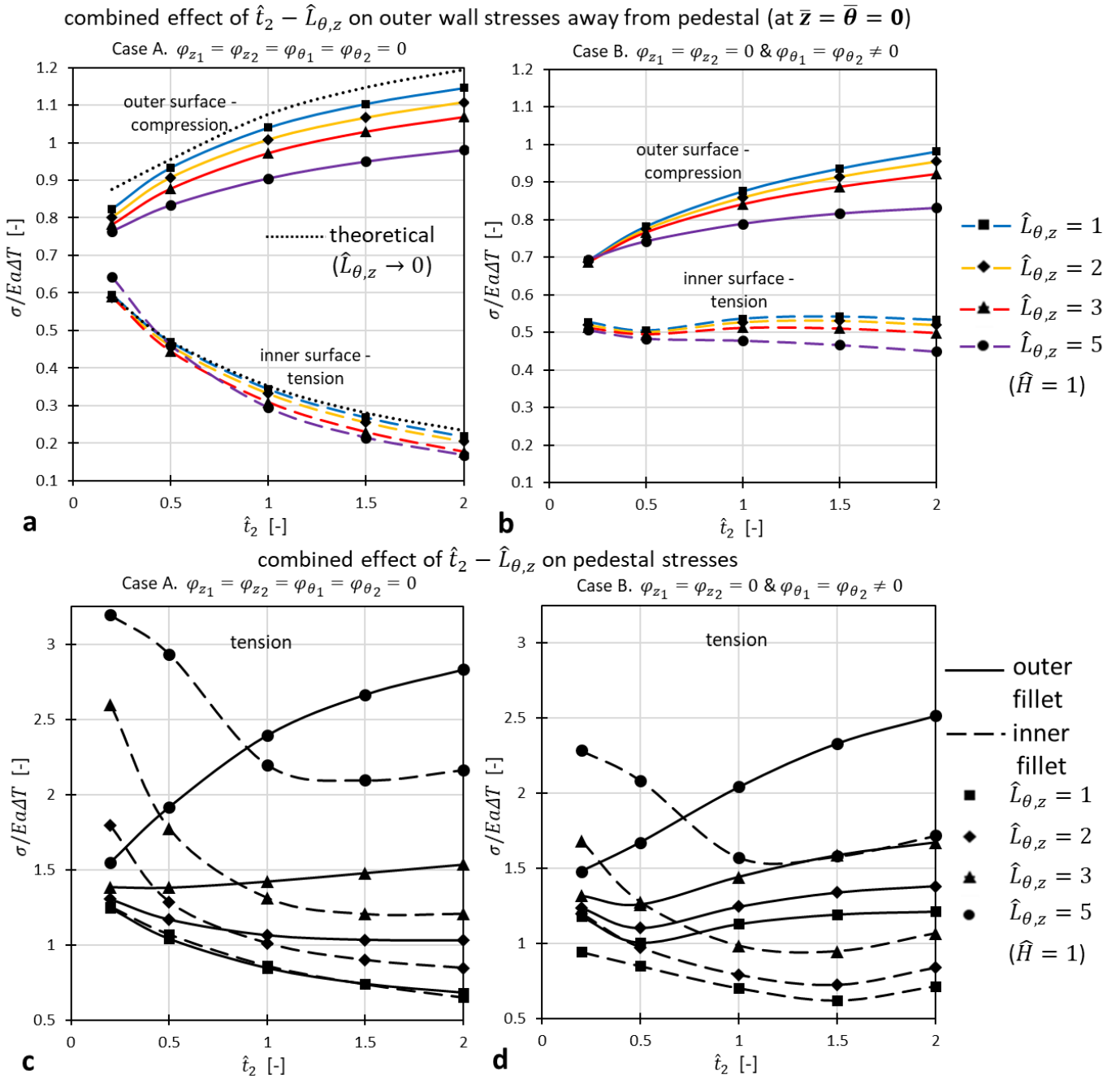


Figure 9. Combined effect of inner wall thickness,  $\hat{t}_2$ , and pedestal spacing,  $\hat{L}_{\theta,z}$ , on critical stresses,  $\sigma$ , for constraint cases A-B, for the unit cell of Figs 8a-b. Plots show: (a-b) compressive and tensile outer wall 1 surface stresses away from the pedestal, at  $\bar{\theta} = \bar{z} = 0$  (see Fig 3), for cases A-B, (c-d) maximum tensile stresses at pedestal fillets for cases A-B. In Fig 9(a), the 3D analytical solution (Equation (7) – Section 2.3.5) is also plotted. Fixed geometric ratios are:  $\hat{R} = 20$ ,  $\hat{H} = \hat{D}_p = 1$ , and  $\hat{\rho}_{Pf} = 0.1$ .

In both cases A-B, the maximum pedestal tensile stresses plotted in Figs 9c-d, occur at different locations along the circumference of the fillets, depending on which of the two stress components,  $\sigma_\theta$  or  $\sigma_z$ , is larger at the corresponding location. This is expected on the basis that the *SCF* is generally higher in the direction normal to the fillet compared to the circumferential direction. Upper bounds for the *SCF* at the outer pedestal fillets can be estimated by dividing the stresses in Figs 9c-d for the minimum pedestal spacing,  $\hat{L}_{z,\theta} = 1$ , by the corresponding nominal tensile stresses in Figs 9a-b. This gives  $SCF = 2.5$  for case A and  $SCF = 2.2$  for case B, on average over the five  $\hat{t}_2$  values studied.

The difference of *SCF* between cases A-B can be the result of several factors, such as the different contributions of membrane forces relative to bending moments on each of the  $\sigma_r$ ,  $\sigma_\theta$  and  $\sigma_z$  components at the fillets, as well as the different magnitudes of these components i.e. different degrees of stress triaxiality. These factors are mainly a function of inner wall thickness,  $\hat{t}_2$ , while for case B, wall spacing,  $\hat{H}$ , also plays an important role.

combined effect of  $\hat{t}_2 - \hat{H}$  on outer wall stresses away from pedestal (at  $\bar{z} = \bar{\theta} = 0$ ), in the absence of a pedestal

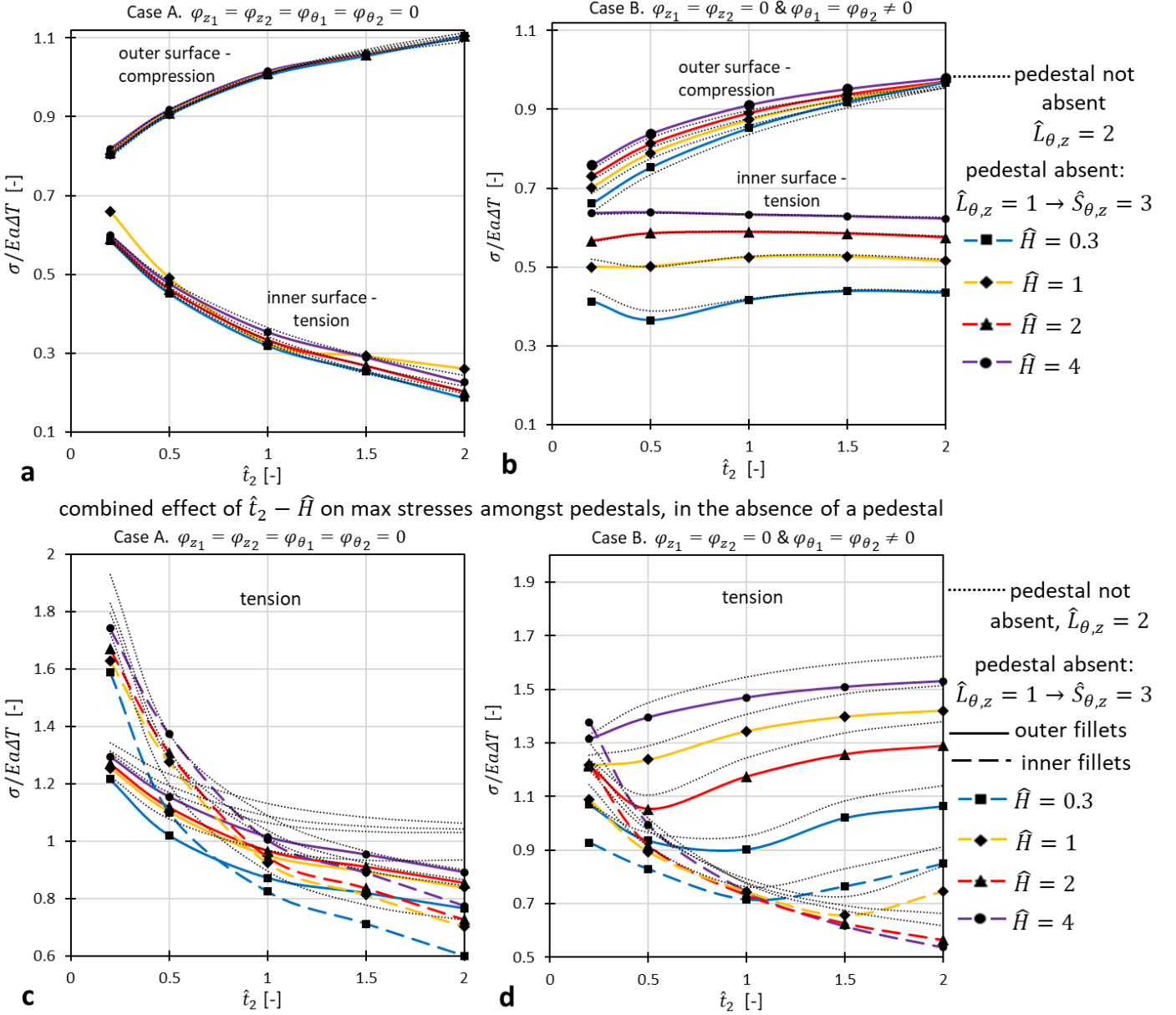


Figure 10. Combined effect of inner wall thickness,  $\hat{t}_2$ , and wall spacing,  $\hat{H}$ , on critical stresses,  $\sigma$ , for cases A-B, for the unit cell of Figs 8a-b. Plots show: (a-b) compressive and tensile outer wall 1 surface stresses away from the pedestal, at  $\bar{\theta} = \bar{z} = 0$  (see Fig 3), for cases A-B, (c-d) maximum tensile stresses at pedestal fillets for cases A-B. Fixed geometric ratios include:  $\hat{R} = 20$ ,  $\hat{L}_{\theta,z} = 2$ ,  $\hat{D}_P = 1$ , and  $\hat{\rho}_{Pf} = 0.1$ .

### 3.3.2 Combined effect of wall thickness and wall spacing

The role of wall spacing,  $\hat{H}$ , combined with the effect of inner wall thickness,  $\hat{t}_2$ , is summarised in Figs 10a-b in terms of outer wall 1 stresses at  $\bar{\theta} = \bar{z} = 0$ , and Figs 10c-d in terms of pedestal stresses. Fixed geometric ratios now include:  $\hat{R} = 20$ ,  $\hat{L}_{z,\theta} = 3$ ,  $\hat{D}_p = 1$ , and,  $\hat{\rho}_{P_f} = 0.1$ . Wall spacing,  $\hat{H}$ , plays a minor role in case A (Figs 10a, c), in agreement with our theoretical analysis in Section 2.3.5. Decreasing  $\hat{H}$  reduces the difference between the outer and inner wall radii,  $R_1$  and  $R_2$ , eventually causing a small decrease in outer wall 1 stresses, and particularly those at the inner surface (see Fig 10a). The considerable decrease of pedestal stresses in Fig 10c for the extreme low value,  $\hat{H} = 0.3$ , is due to the above effect, superimposed on the effect of the interaction between stress concentrations in the upper and lower fillets (decreasing SCFs).

On the other hand, in case B, wall spacing,  $\hat{H}$ , is a critical parameter with the primary effect of increasing both compressive and tensile stresses in the outer wall 1 (Fig 10b), and thus stresses in the outer pedestal fillet (Fig 10d); the effect is more pronounced at low  $\hat{H}$ . The trend is underpinned by the 2D solution for the condition,  $\varphi_{\theta_1} = \varphi_{\theta_2} \neq 0$ , in Section 2.3.1, where decreasing  $\hat{H}$  converts the membrane forces,  $N_{z_1}$  and  $N_{z_2}$ , into bending moments,  $M_{\theta_1}$  and  $M_{\theta_2}$ , in both walls. The reason why the effect of  $\hat{H}$  on compressive stresses gradually diminishes with increasing  $\hat{t}_2$  (see Fig 10b), is because at large  $\hat{t}_2$ , the  $\sigma_\theta$  stresses induced by the constraint  $\varphi_{z_1} = \varphi_{z_2} = 0$ , which are insensitive to  $\hat{H}$ , dominate over  $\sigma_z$  stresses associated with the  $\varphi_{\theta_1} = \varphi_{\theta_2} \neq 0$  condition. In a similar manner, the combined effect of  $\hat{t}_2 - \hat{H}$  ratios on the pedestal fillet stresses in Fig 10d, changes because whether the constraint  $\varphi_{z_1} = \varphi_{z_2} = 0$  or  $\varphi_{\theta_1} = \varphi_{\theta_2} \neq 0$  dominates depends on the precise values of  $\hat{t}_2$  and  $\hat{H}$ . Similar to Section 3.3.1, we find that an independent 2D analysis for each constraint provides the means for interpreting the role of primary geometric features,  $\hat{t}_2$ ,  $\hat{H}$  and  $\hat{L}_{z,\theta}$ , on the 3D behaviour.

## 3.4 Role of detailed geometric features - pedestal characteristics

### 3.4.1 Pedestal shape

We now explore detailed 3D effects, such as the impact of pedestal shape on mechanical performance. We compare the circular pedestal cross section used so far (Fig 11a), against a square section (Fig 11b) as well as a square section rotated by  $45^\circ$  about the  $r$  axis (Fig 11c). Non-circular sections are of interest from a cooling perspective, because they can modify heat conduction between the two walls, but more importantly promote turbulence in the coolant flow which enhances internal convection. The three sections (Fig 11a-c) are compared as a function of pedestal-wall fillet radius,  $\hat{\rho}_{P_f}$ , and fixed pedestal size,  $\hat{D}_p = 1$ ; square sections (Figs 11b-c), also involve a longitudinal fillet of constant radius,  $\hat{q}_{P_f} = \varrho_{P_f}/t_1 = 0.1$ , whereas  $\hat{D}_p$  now represents edge length (instead of diameter). Primary geometric ratios are also fixed ( $\hat{R} = 20$ ,  $\hat{L}_{z,\theta} = 2$ ,  $\hat{t}_2 = \hat{H} = 1$ ).

For both types of constraint, the square rotated section clearly gives the highest fillet stresses (see Figs 11e-f) and highest stress concentration factors,  $SCF$  (Fig 11d); differences in  $SCF$  (Fig 11d) and stresses (Figs 11e-f) between the circular and square sections are small, and are only evident for sharp fillets i.e.  $\hat{q}_{P_f} < 0.1$ . We use an upper bound value for  $SCF$  in Fig 11d here, obtained by driving the stresses in Figs 11e-f, by the corresponding nominal tensile stresses at  $\bar{\theta} = \bar{z} = 0$  in Figs 9a-b, for

$\hat{L}_{z,\theta} = 2$  and  $\hat{t}_2 = 1$ . Since for a curved geometry the nominal tensile stresses at  $\bar{\theta} = \bar{z} = 0$  are lower than the ones corresponding to the critical location of the pedestal fillet, the upper bound values presented in Fig 11d can be overly conservative and should be generally interpreted with caution. For a more accurate determination of  $SCF$  based on the nominal FE stresses at  $\bar{\theta} = \bar{z} = 0$ , one should use a unit cell with very small curvature i.e.  $\hat{R} > 100$ , in order to minimise the variation of nominal stresses with position from the pedestal. Alternatively, our theoretical solution in Eq (7) can be used, given also the fact that the accuracy of this solution increases at large  $\hat{R}$ . Previous work in axisymmetric unit cells with pedestal diameter  $\hat{D}_p = 1$  reported values of  $SCF = 1.95$  and  $SCF = 2.35$  for  $\hat{q}_{P_f} = 0.1$  and  $\hat{q}_{P_f} = 0.05$ , respectively [55]; for  $\hat{D}_p = 0.5$  these values decreased to  $SCF = 1.7$  and  $SCF = 1.95$  for  $\hat{q}_{P_f} = 0.1$  and  $\hat{q}_{P_f} = 0.05$ . Note, however, that these values should also be interpreted with caution as the value of  $SCF$  at a pedestal fillet is generally sensitive to the nominal stress distribution through the wall thickness i.e. the contributions of bending moment and membrane force. This implies that different  $SCFs$  apply between the inner and outer pedestal fillet, since the two walls experience different nominal stresses distributions, particularly in the constraint case A where the inner wall is subjected into pure tension. Indeed, Fig 11d indicates that case A leads to a significantly higher  $SCF$  than case B, although in the latter the actual fillet stresses are slightly larger (compare Figs 11e-f). Detailed phenomena at pedestal fillets will be investigated in subsequent studies based on stress distributions arising from more detailed temperature fields. The purpose here is to explore whether pedestal shape plays an important role in terms of structural integrity.

The peak stress location in the square sections (Figs 11b-c) consistently lies at the corner/intersection between the pedestal-wall fillet and longitudinal fillet. This observation, combined with the fact that  $\sigma_z$  stresses are slightly larger than  $\sigma_\theta$  (for the specific  $\hat{t}_2 = \hat{H} = 1$  ratios considered here) for both A and B, explains the increase in  $SCF$  upon rotating the square section by  $45^\circ$ ; again, this is on the basis that the  $SCF$  is always higher in the direction normal to the fillet compared to the direction along the peripheral of the fillet. From a practical point of view, the cross-sectional shape is less important than the fillet radius,  $\hat{p}_{P_f}$ , in determining the  $SCF$  (Fig 11d) and corresponding stresses (Figs 11e-f). This indicates that mechanical performance at pedestals relies largely on the manufacturing capability of producing large pedestal-wall fillet radii. The role of longitudinal fillet in the square sections (Figs 11b-c) is found to be less important, i.e. the results of Figs 11d-e only change by a maximum of 3% upon reducing  $\hat{R}_{P_f}$  from 0.1 into 0.05 (not shown).

We now investigate the effect of pedestal size. In terms of heat transfer, larger pedestals promote thermal conduction between the walls, enhancing overall cooling performance. From a solid mechanics perspective, however, previous 2D analyses have shown that thin pedestals tend to reduce stress at the fillets. The detailed effect of circular pedestal diameter,  $\hat{D}_p$ , on pedestal stresses, as a function of pedestal spacing,  $\hat{L}_{z,\theta}$ , is illustrated in Figs 12a-b. Fixed geometric ratios include:  $\hat{R} = 20$ ,  $\hat{t}_2 = \hat{H} = 1$ ,  $\hat{p}_{P_f} = 0.1$ . The feature of decreasing stress in the outer and inner fillets with decreasing  $\hat{D}_p$  is evident in both constraint cases A-B (Figs 12a-b). Decreasing  $\hat{D}_p$  however, below a critical size, almost instantly degrades the performance, as both fillets experience the same dramatic increase in tensile stress. The larger the pedestal spacing,  $\hat{L}_{z,\theta}$ , the larger the critical pedestal size.

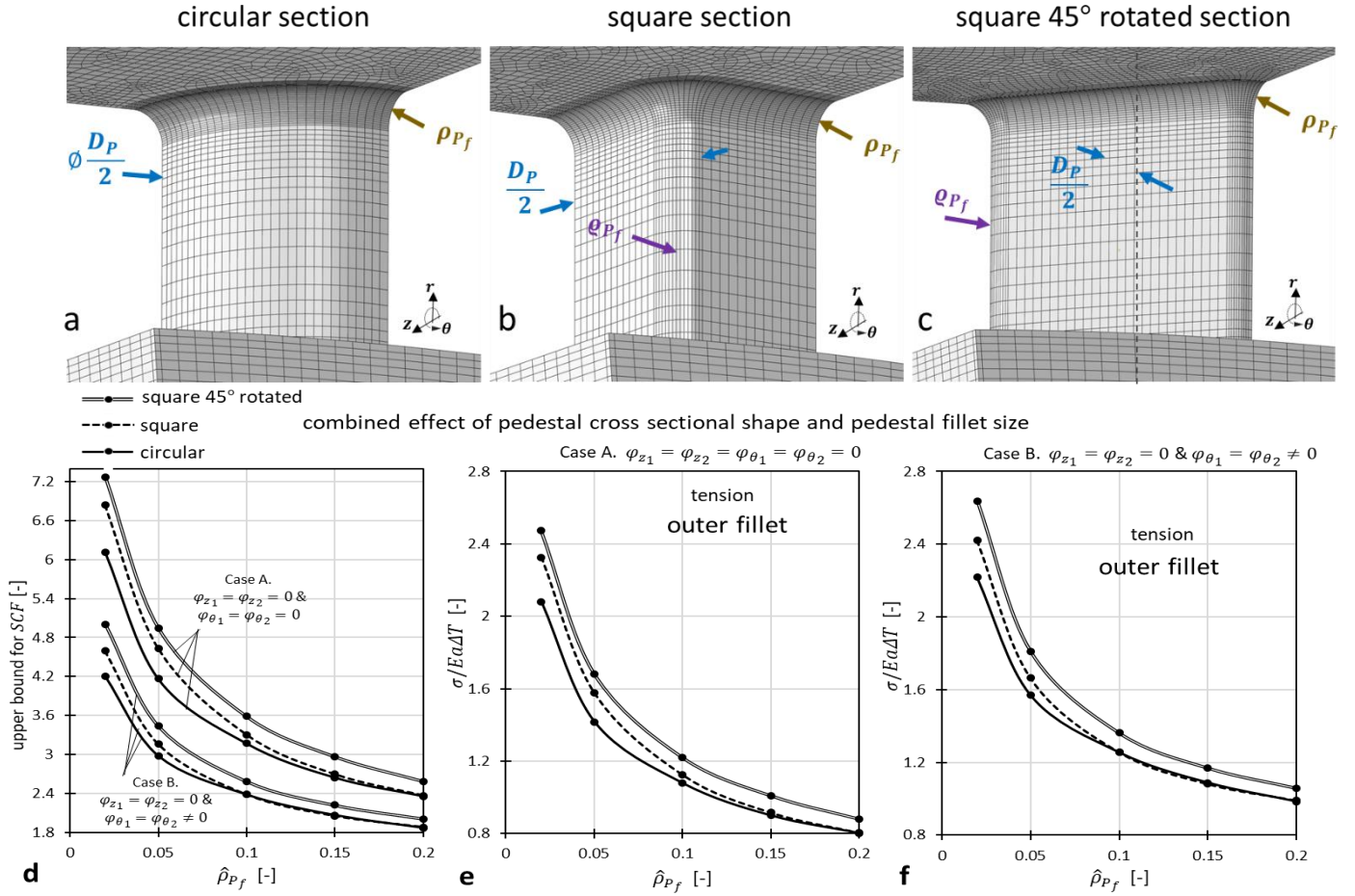


Figure 11. Combined effect of pedestal cross sectional shape and pedestal fillet radius,  $\hat{\rho}_{Pf}$ , on maximum stresses at the outer pedestal fillet. Images (a), (b) and (c) show meshed FE models of pedestals with circular section, square section and square section rotated 45° about the  $r$  axis, respectively (for the unit cell of Figs 8a-b). Plots show: (d) conservative stress concentration factor,  $SCF$ , calculations as a function of  $\hat{\rho}_{Pf}$ , for the three pedestal sections in (a-c), for constraint cases A-B, (e-f) local stresses for the sections in (a-c) for cases A-B. Fixed geometric ratios are:  $\hat{R} = 20$ ,  $\hat{L}_{\theta,z} = 2$ ,  $\hat{t}_2 = \hat{H} = \hat{D}_P = 1$ , and  $\hat{\rho}_{Pf} = 0.1$ .

### 3.4.2 Pedestal size

This is again explained by our theoretical 2D analysis of coupled rings in Section 2.3.3, which is relevant to the  $r - \theta$  plane of the 3D unit cell. Specifically, the pedestal carries a purely tensile force that constrains the potential increase in the relative radial distance between the two walls; this is on top of transmitting shear forces and bending moments. The pedestal cross sectional area that carries this tensile force decreases quadratically with  $\hat{D}_P$ , thus if the tensile constraining force is independent of pedestal size we would expect to see a corresponding increase in the axial stress in the pedestal with decreasing pedestal size. For this regime, FE simulations verified that the tensile force dominates, such that the pedestal is practically subjected into tension. For the 3D case here, the critical tensile force effectively scales with the membrane force (per unit length) that is generated in the two walls, multiplied by the pedestal spacing,  $\hat{L}_{z,\theta}$ . Thus, in both cases A-B, the tensile force through the pedestal increases with either increasing  $\hat{L}_{z,\theta}$  and/or  $\hat{t}_2$  (and/or increasing  $\hat{H}$  for case B). This is indeed confirmed by Figs 13a-d, where similar to the combined role of  $\hat{D}_P - \hat{L}_{z,\theta}$  in Figs 12a-b, increasing  $\hat{t}_2$  necessitates a larger pedestal diameter,  $\hat{D}_P$ , in order to avoid overstressing the pedestal.

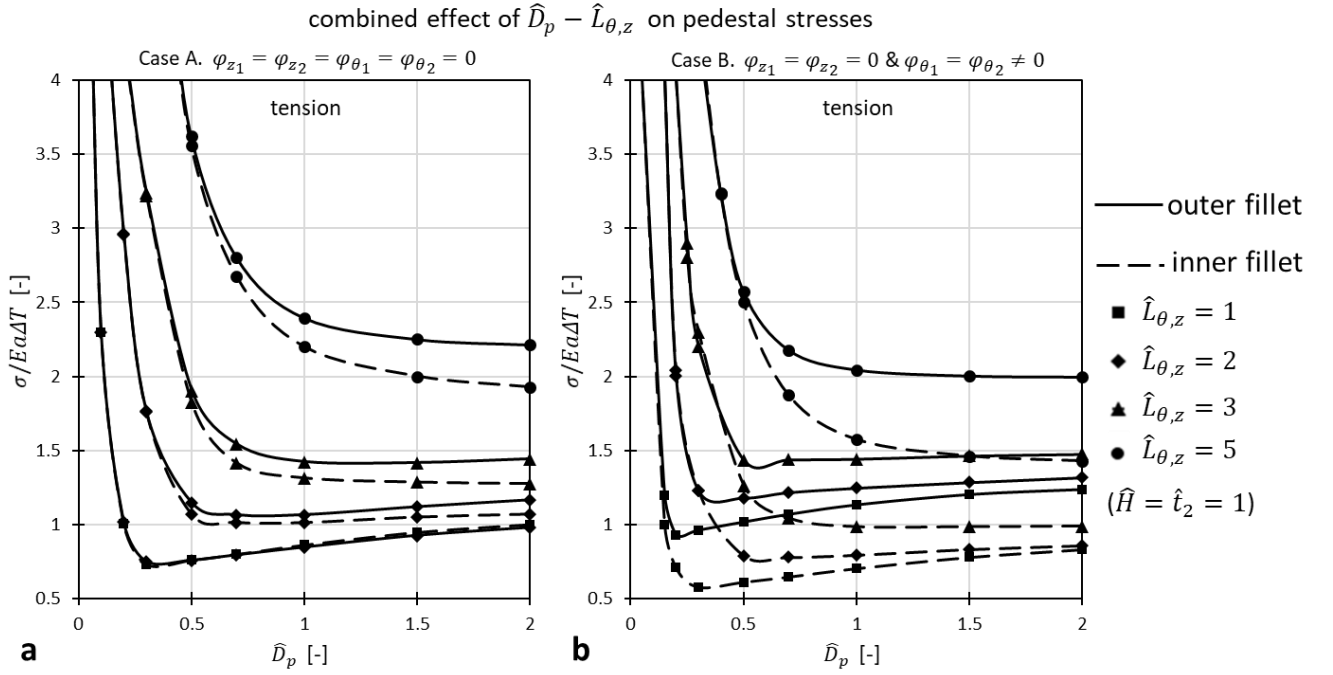


Figure 12. Combined effect of pedestal diameter,  $\hat{D}_p$  (circular section) and pedestal spacing,  $\hat{L}_{\theta,z}$ , on maximum pedestal stresses for constraint case A (a) and case B (b) (unit cell in Figs 8a-b). Fixed geometric ratios include:  $\hat{R} = 20$ ,  $\hat{t}_2 = \hat{H} = 1$ , and  $\hat{\rho}_{Pf} = 0.1$ .

### 3.5 Changing design - absence of a pedestal

#### 3.5.1 Stress field with some pedestals removed to accommodate effusion and impingement holes

So far, we have analysed primary and detailed geometric effects by using an elementary unit cell that represents the simplest form of connection between two walls, i.e. via equally spaced pedestals (Fig 8). We will now explore whether the phenomena and trends discussed so far also apply in more complex forms of connection. Here we modify the design, by adopting the double wall concept for turbine blades shown in Fig 1a. By excluding holes, as well as by considering the same geometric idealisation of concentric cylindrical walls (constant external curvature,  $\hat{R} = 20$ ), this concept differs from the elementary unit cell used so far (Fig 8), mainly in that some pedestals are removed, in a periodic manner, to accommodate the effusion and impingement holes in the outer and inner walls, respectively (see Fig 1a). Therefore, we modify the unit cell in Fig 8 to produce the new representative unit cell shown in Figs 14a-d, for which the same form of temperature field and combined structural constraints, i.e. cases A-B, are applied (as described in Section 2.4).

The stress contours shown in Figs 14a-b correspond to the case of a hot temperature applied on the convex outer surface of the unit cell, whereas Figs 14c-d concern the scenario of a hot temperature applied on the concave outer surface of the unit cell (in which the reference to outer wall 1 and inner wall 2 is inverted); the latter will be discussed in Section 3.5.2.2. Figs 14a-d illustrate the deformed configuration using a deformation scale factor of 50. The geometric ratios used in the simulations are:  $\hat{R} = 20$ ,  $\hat{L}_{\theta,z} = 2$ ,  $\hat{t}_2 = \hat{H} = \hat{D}_p = 1$ ,  $\hat{\rho}_{Pf} = 0.1$ . The lengths  $\hat{L}_{\theta,z} = \hat{L}_\theta = \hat{L}_z = 2$  and  $\hat{D}_p = 1$  used here relate to the ‘secondary’ pedestal spacings in the  $\bar{\theta} = 0$  and  $\bar{z} = 0$  planes, respectively through  $\hat{S}_\theta = 2\hat{L}_\theta + \hat{D}_p = 5$  and  $\hat{S}_z = 2\hat{L}_z + \hat{D}_p = 5$ .



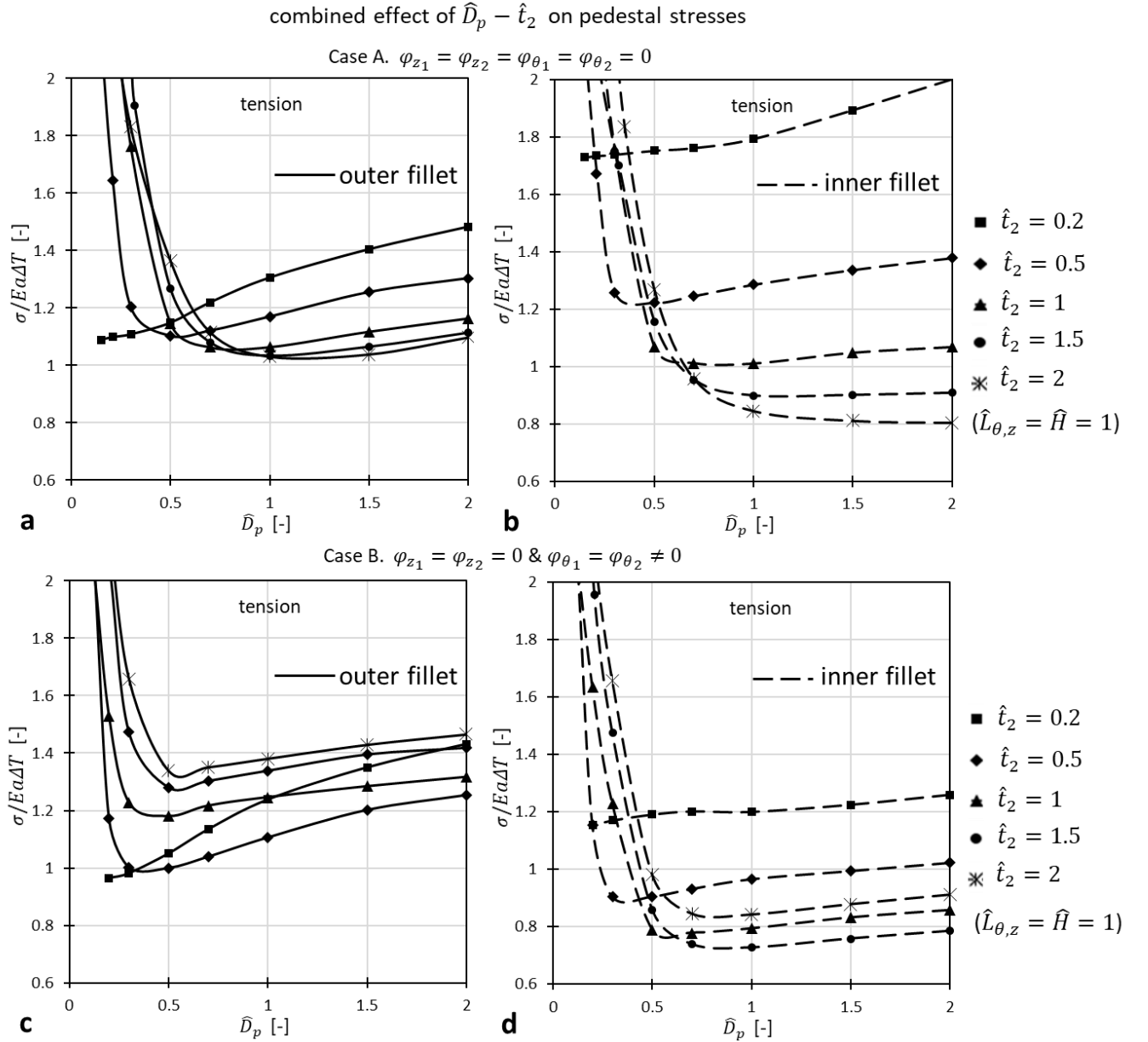


Figure 13. Combined effect of pedestal diameter,  $\hat{D}_p$  (circular section) and inner wall thickness,  $\hat{t}_2$ , on maximum pedestal stresses in the outer and inner fillets for constraint case A (a-b) and case B (c-d) (unit cell in Figs 8a-b). Fixed geometric ratios include:  $\hat{R} = 20$ ,  $\hat{L}_{\theta,z} = \hat{H} = 1$ , and  $\hat{\rho}_{Pf} = 0.1$ .

The major differences in the stress fields between constraint cases A-B in Figs 14a-b are equivalent to those for the simpler unit cell considered in Figs 8a-b. Case A leads to larger compressive stresses in the outer surface of wall 1 (Fig 14a) and larger pedestal fillet stresses on average between the outer and inner fillets. The maximum pedestal stresses mainly occur at the pedestal in the  $\bar{\theta} = 0$  plane; stresses at the pedestal at  $\bar{z} = 0$  are of similar order, whereas the pedestal near  $\bar{\theta} = \bar{z} = 0$  experiences considerably lower stresses than the other pedestals. These are associated with ‘secondary’ pedestal spacing,  $\hat{S}_{\theta,z} = 2\hat{L}_{z,\theta} + \hat{D}_p$ , which is larger than  $\hat{L}_{z,\theta}$  and essentially dictates the variation of maximum pedestal stresses with pedestal spacing. Another common feature with Figs 8a-b is that in Figs 14a-b, the compressive stresses at the outer surface of wall 1 decrease with distance from the pedestal, especially at  $\bar{\theta} = \bar{z} = 0$ , which is relevant to the effusion hole location. The variation of stresses throughout the system is illustrated in more detail

within Figs 15a-b, where in both cases A-B, the outer surface compressive stresses are shown to increase with pedestal spacing,  $\hat{L}_{\theta,z}$ , at locations above all pedestals, and decrease at the location away from pedestal,  $\bar{\theta} = \bar{z} = 0$ , associated with the effusion hole. Figs 15a-b for the case where a pedestal is absent, are consistent with the corresponding plots in Figs 7a-b for the simpler unit cell, in that case again case A gives higher compressive stresses and lower tensile stresses than case B. This relates to the fact that similar stress ratios,  $\sigma_z/\sigma_\theta$ , to those observed in Figs 7c-d are obtained in Figs 15c-d; these mainly involve nearly equibiaxial states ( $\sigma_z/\sigma_\theta \approx 1$ ) for case A, whereas for case B,  $\sigma_z > \sigma_\theta$  in the tensile outer wall surface and  $\sigma_z < \sigma_\theta$  throughout the compressive surface. These observations, suggest that different pedestal arrangements, such as the case here when pedestals are removed in a periodic manner (Fig 14), do not change the main features of the double wall response.

The argument is further supported by Fig 16, which shows the combined effect of skin thickness,  $\hat{t}_2$ , and wall spacing,  $\hat{H}$ , on the outer wall 1 stresses at  $\bar{\theta} = \bar{z} = 0$  (Figs 16a-b), as well as on the maximum outer fillet and inner fillet stresses for all pedestals (Figs 16c-d); the corresponding results of Fig 10 (when all pedestals are present), for  $\hat{L}_{z,\theta} = 2$ , are also plotted here (dotted lines) for comparison. Fixed geometric ratios include:  $\hat{R} = 20$ ,  $\hat{L}_{z,\theta} = \hat{D}_P = 1$  ( $\hat{S}_{\theta,z} = 3$ ) and  $\hat{\rho}_{Pf} = 0.1$ . Clearly, the absence of a pedestal does not qualitatively change the combined effect of  $\hat{t}_2 - \hat{H}$  on critical stresses, but it changes the stress magnitudes, particularly at the pedestal fillets. In particular, the ‘secondary’ pedestal spacing,  $\hat{S}_{\theta,z} = 2\hat{L}_{z,\theta} + \hat{D}_P$ , changes how the stress field varies with distance from the pedestals, as well as the sensitivity with respect to pedestal spacings,  $\hat{L}_{z,\theta}$ , and/or  $\hat{S}_{\theta,z}$ . This is a new feature that comes into play here when some pedestals are absent, and more generally, when pedestal arrangement is changed.

We demonstrate this aspect further in Figs 17a-b, which compares the sensitivity of outer wall 1 stresses at the effusion hole location,  $\bar{\theta} = \bar{z} = 0$ , with respect to pedestal spacing, the elementary unit cell (i.e. all pedestals present (Figs 8a-b)) and the case when some pedestals are removed (Figs 14a-b); for the latter case, the ‘secondary’ pedestal spacing,  $\hat{S}_{\theta,z}$ , is taken as the relevant spacing in the plots. So far in our study, pedestal spacing has been varied simultaneously in both directions i.e.  $\hat{L}_{z,\theta}$ , and,  $\hat{S}_{\theta,z}$ ; here in Figs 17a-b, these spacings are varied individually in the  $\theta$  ( $\hat{L}_\theta, \hat{S}_\theta$ ) and  $z$  ( $\hat{L}_z, \hat{S}_z$ ) directions, while keeping the spacing in the other direction constant. Fixed geometric ratios include:  $\hat{R} = 20$ ,  $\hat{t}_2 = \hat{H} = \hat{D}_P = 1$ ,  $\hat{\rho}_{Pf} = 0.1$ . In both constraint cases A-B, the important feature is that when some of the pedestals are removed, varying pedestal spacing individually in one direction i.e. either  $\hat{S}_\theta$  or  $\hat{S}_z$ , has a detrimental effect on the tensile and compressive stresses in the outer wall (see Figs 17a-b). In the elementary unit cell, increasing spacing in any manner i.e. either  $\hat{L}_\theta, \hat{L}_z$  or  $\hat{L}_{z,\theta}$ , reduces the compressive stresses (see Figs 17a-b). However, in both cases, the different degree of influence of pedestal spacing in the  $\theta$  and  $z$  directions arises only in the large pedestal spacing regime, which is not of interest for the transpiration cooling systems considered here.

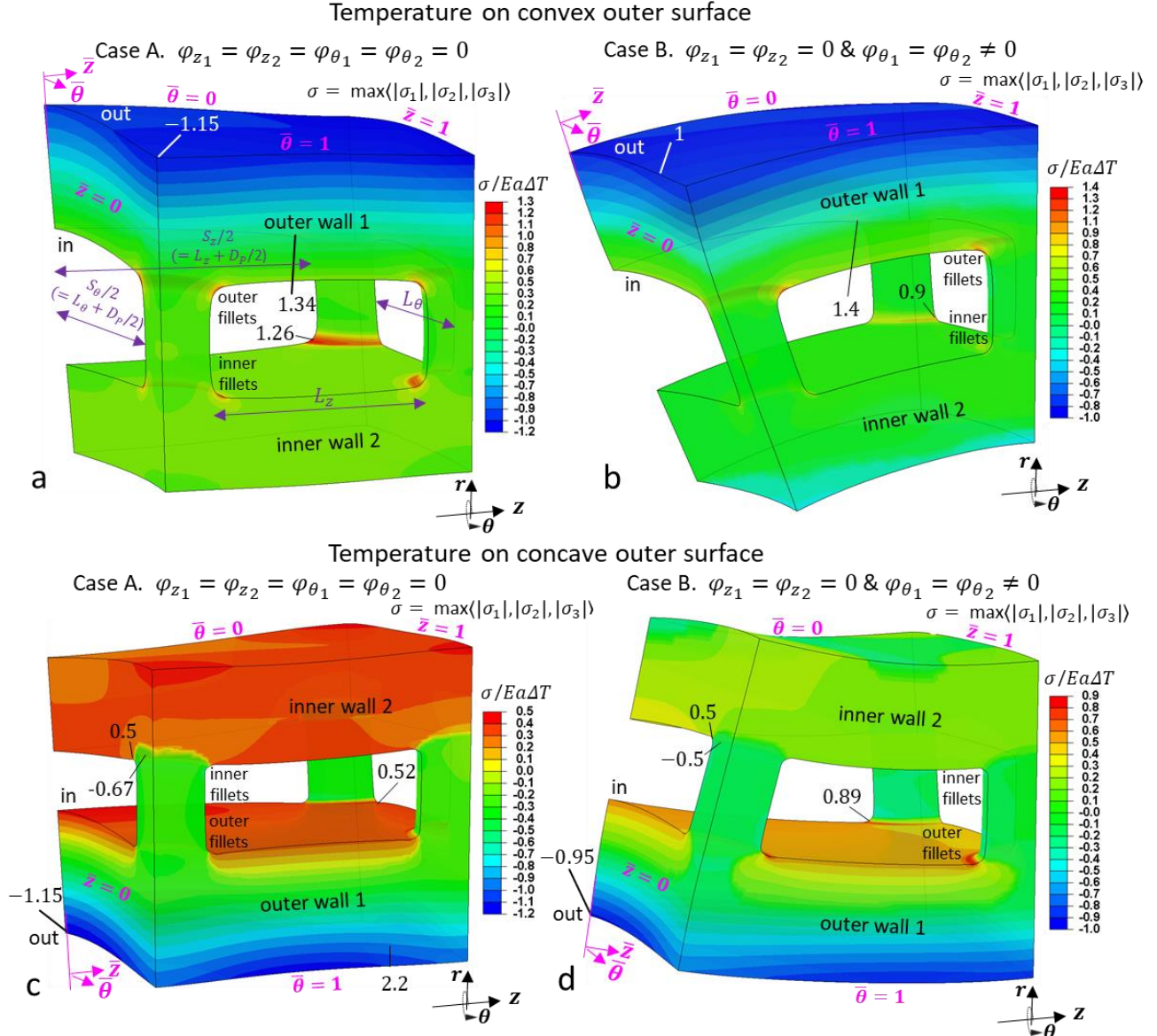


Figure 14. Comparison of 3D FE thermal stress fields in double walls where the connecting pedestals are periodically absent; maximum absolute principal stresses,  $\sigma$ , normalised with respect to  $Ea\Delta T$ . (a-b) correspond to constraint cases A-B for a hot temperature applied on the convex outer surface of the cylindrical double wall system (to be compared with Figs 8a-b), and (c-d) correspond to cases A-B for a hot temperature applied on the concave outer surface of the system. Geometric ratios include:  $\hat{R} = 20$ ,  $\hat{L}_{\theta,z} = 2$ ,  $\hat{t}_2 = \hat{H} = \hat{D}_P = 1$ , and  $\hat{\rho}_{Pf} = 0.1$ ; pedestal spacings in the  $\bar{\theta} = 0$  and  $\bar{z} = 0$  planes are respectively,  $\hat{S}_{\theta} = 2\hat{L}_{\theta} + \hat{D}_P = 5$  and  $\hat{S}_z = 2\hat{L}_z + \hat{D}_P = 5$ . Critical compressive and tensile stress are denoted alongside the contours.

### 3.5.2 Pedestal size effects in the absence of a pedestal – convex/concave surfaces

#### 3.5.2.1 Temperature on convex outer surface

In this final section, we explore the implications of the removal of a pedestal from the unit cell on the minimum pedestal size requirements. For cases A-B, Figs 17a-b show the combined effect of pedestal diameter,  $\hat{D}_P$ , and pedestal spacing,  $\hat{L}_{z,\theta}$ , on the outer and inner pedestal fillet stresses when a pedestal is removed (i.e. Figs 14a-b), in comparison with the corresponding results for the elementary unit cell in Figs 12a-b i.e. full population of pedestals. Similar to the combined effect of

primary geometric features,  $\hat{t}_2 - \hat{H}$  (shown earlier in Fig 16), the effect of  $\hat{L}_{z,\theta} - \hat{D}_p$  qualitatively remains the same when pedestals are removed, in that increasing pedestal spacing,  $\hat{L}_{z,\theta}$ , increases the critical  $\hat{D}_p$  value below which stresses increase sharply (see Figs 18a-b). The difference here is that in the regime above each critical  $\hat{D}_p$  value, stresses increase considerably with pedestal size; this effect is not at play in the case of a full population of pedestals i.e. pedestal not absent. The increase of stresses with increasing  $\hat{D}_p$  is attributed to the fact that when a pedestal is omitted, increasing  $\hat{D}_p$  also increases  $\hat{S}_{\theta,z}$  (according to  $\hat{S}_{\theta,z} = 2\hat{L}_{z,\theta} + \hat{D}_p$ ), which is the controlling pedestal spacing parameter for the maximum pedestal stresses (Section 3.5.1). This generally suggests that for the double wall concept in Figs 14a-b, it is more convenient to use  $\hat{S}_{\theta,z}$  instead of  $\hat{L}_{z,\theta}$ , as the most significant dimension for design considerations.

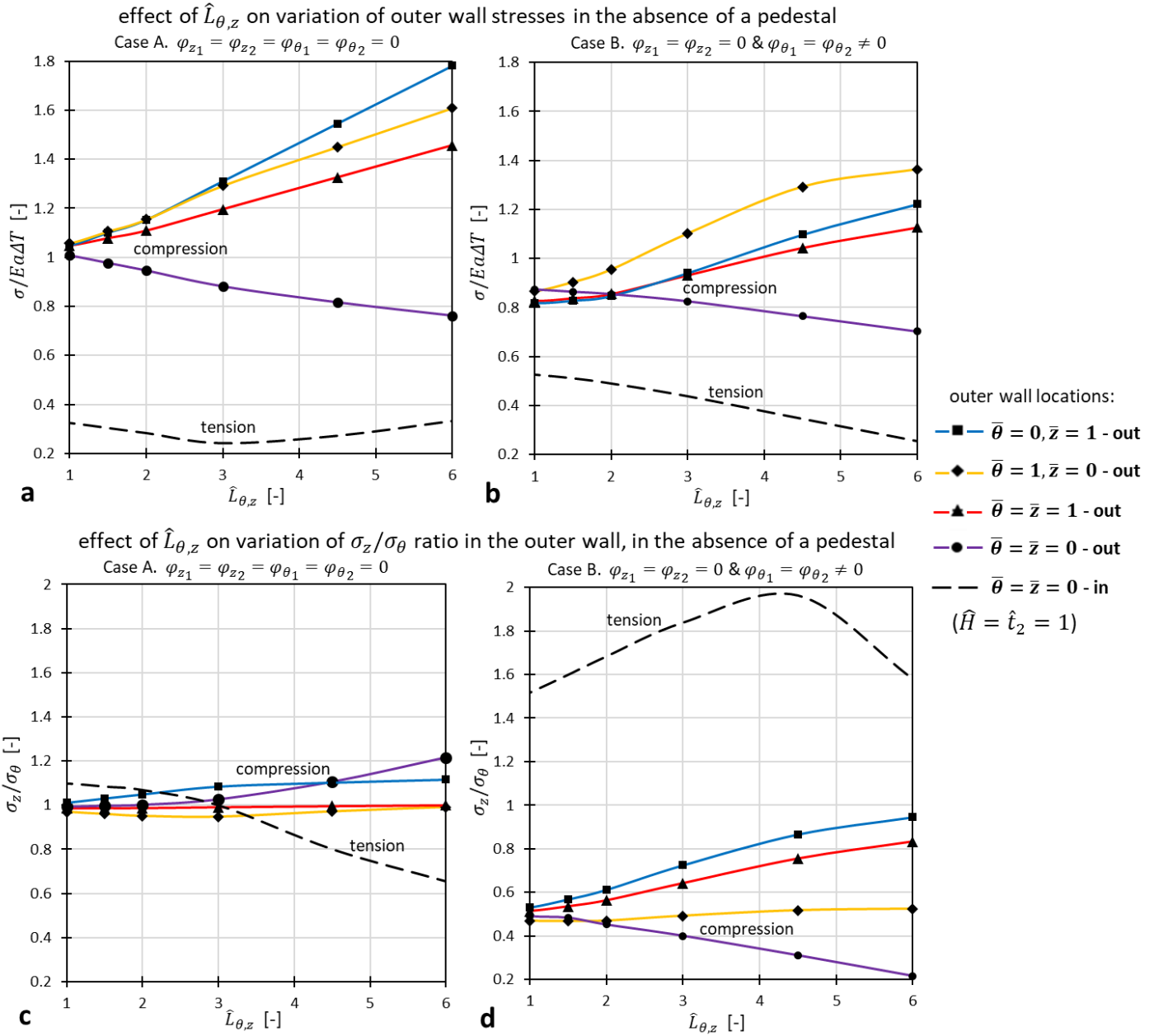


Figure 15. Variation of stress states at characteristic surface points of the double wall system of Figs 14a-b where pedestals are periodically removed, for constraint cases A-B. (a-b) show the effect of pedestal spacing,  $\hat{L}_{\theta,z}$ , on compressive and tensile stresses,  $\sigma$ , at various locations of the outer wall 1, for cases A-B, and, (c-d) show the effect of pedestal spacing,  $\hat{L}_{\theta,z}$ , on the stress ratio,  $\sigma_z/\sigma_\theta$ , at the same outer wall 1 locations for cases A-B. Fixed geometric ratios include:  $\hat{R} = 20$ ,  $\hat{t}_2 = \hat{H} = \hat{D}_p = 1$  and  $\hat{\rho}_{pf} = 0.1$ .

combined effect of  $\hat{t}_2 - \hat{H}$  on outer wall stresses away from pedestal (at  $\bar{z} = \bar{\theta} = 0$ ), in the absence of a pedestal

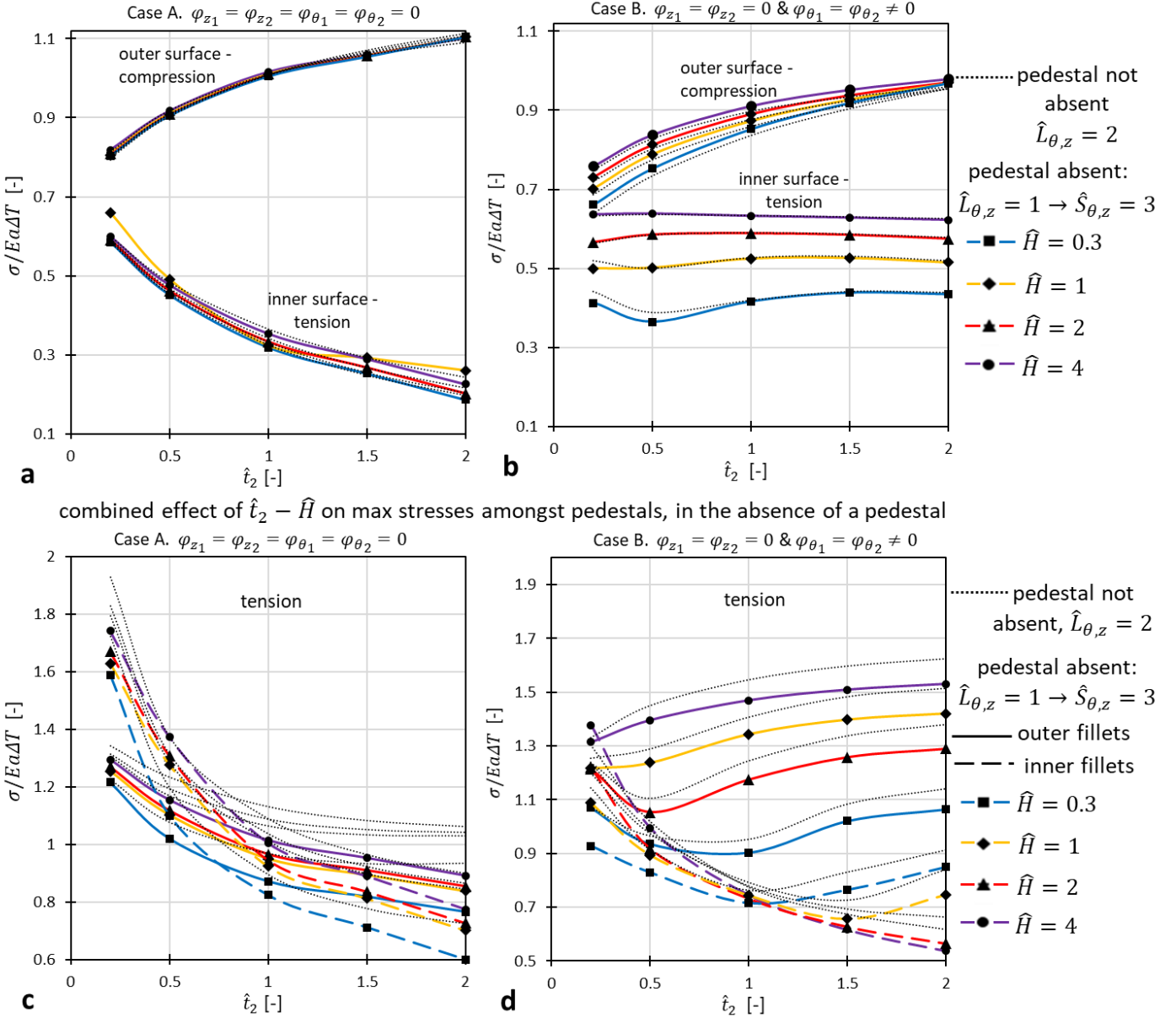


Figure 16. Combined effect of inner wall thickness,  $\hat{t}_2$ , and wall spacing,  $\hat{H}$ , on critical stresses,  $\sigma$ , for constraint cases A-B, for the double wall system of Figs 14a-b, where pedestals are periodically absent. (a-b) show compressive and tensile outer wall 1 stresses away from pedestal, at  $\bar{\theta} = \bar{z} = 0$ , for cases A-B. (c-d) show tensile stresses at pedestal fillets for cases A-B. Fixed geometric ratios include:  $\hat{R} = 20$ ,  $\hat{L}_{\theta,z} = 2$ ,  $\hat{D}_p = 1$  ( $\hat{S}_{\theta,z} = 2\hat{L}_{\theta} + \hat{D}_p = 5$ ) and  $\hat{\rho}_{Pf} = 0.1$ . The corresponding results for the unit cell of Figs 8a-b (which contains a full set of pedestals) for  $\hat{L}_{\theta,z} = 2$  are also plotted – dotted lines.

In this final section, we explore the implications of the removal of a pedestal from the unit cell on the minimum pedestal size requirements. For cases A-B, Figs 17a-b show the combined effect of pedestal diameter,  $\hat{D}_p$ , and pedestal spacing,  $\hat{L}_{z,\theta}$ , on the outer and inner pedestal fillet stresses when a pedestal is removed (i.e. Figs 14a-b), in comparison with the corresponding results for the elementary unit cell in Figs 12a-b i.e. full population of pedestals. Similar to the combined effect of primary geometric features,  $\hat{t}_2 - \hat{H}$  (shown earlier in Fig 16), the effect of  $\hat{L}_{z,\theta} - \hat{D}_p$  qualitatively remains the same when pedestals are removed, in that increasing pedestal spacing,  $\hat{L}_{z,\theta}$ , increases the critical  $\hat{D}_p$  value below which stresses increase sharply (see Figs 18a-b). The difference here is that



in the regime above each critical  $\hat{D}_p$  value, stresses increase considerably with pedestal size; this effect is not at play in the case of a full population of pedestals i.e. pedestal not absent. The increase of stresses with increasing  $\hat{D}_p$  is attributed to the fact that when a pedestal is omitted, increasing  $\hat{D}_p$  also increases  $\hat{S}_{\theta,z}$  (according to  $\hat{S}_{\theta,z} = 2\hat{L}_{z,\theta} + \hat{D}_p$ ), which is the controlling pedestal spacing parameter for the maximum pedestal stresses (Section 3.5.1). This generally suggests that for the double wall concept in Figs 14a-b, it is more convenient to use  $\hat{S}_{\theta,z}$  instead of  $\hat{L}_{z,\theta}$ , as the most significant dimension for design considerations.

effect of pedestal spacing in  $\theta$  and  $z$  directions, on outer wall stresses away from pedestals (at  $\bar{z} = \bar{\theta} = 0$ ), in the absence of a pedestal

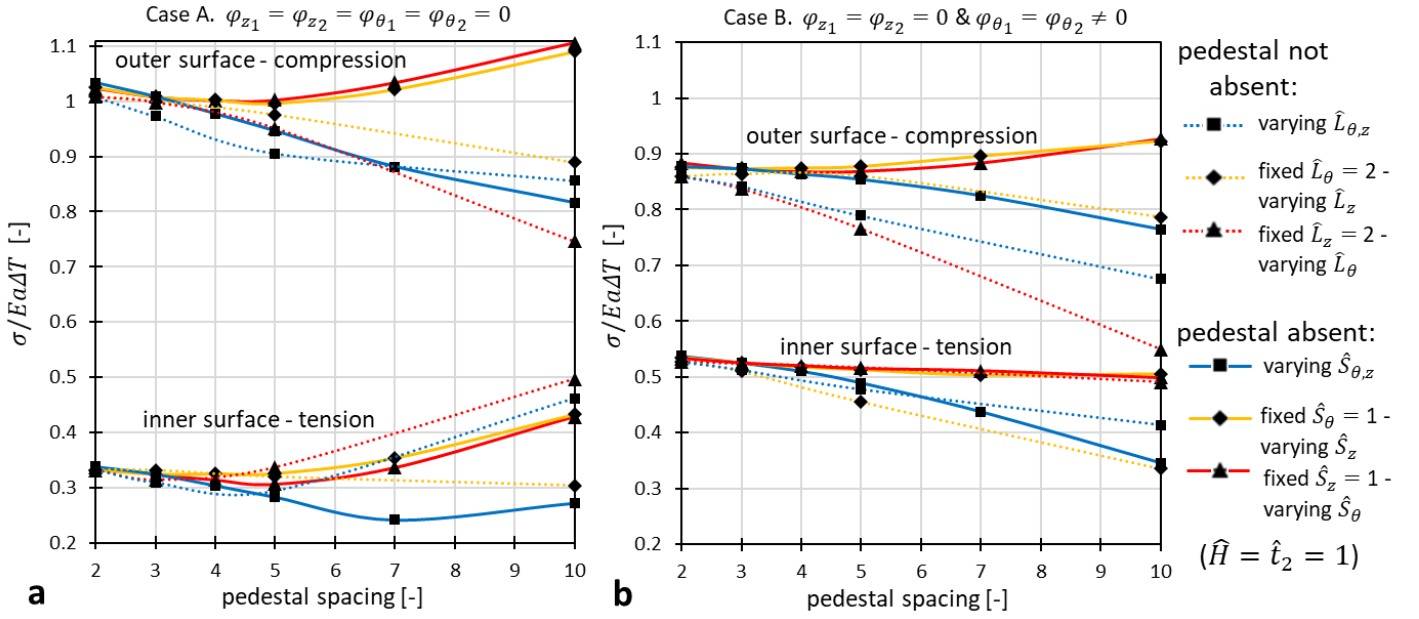


Figure 17. Detailed effect of pedestal spacing in  $\theta$  and  $z$  directions, on outer wall 1 critical stresses away from a pedestal, at  $\bar{\theta} = \bar{z} = 0$ , between double walls designs where pedestals are periodically absent (unit cell of Figs 14a-b) and not absent (unit cell of Figs 8a-b), for constraint case A (a) and case B (b). When some pedestals are absent, the parameters  $\hat{S}_{\theta,z}$ ,  $\hat{S}_\theta$ , and  $\hat{S}_z$  are used for the pedestal spacing in the plots. Fixed geometric ratios include:  $\hat{R} = 20$ ,  $\hat{t}_2 = \hat{H} = \hat{D}_p = 1$  and  $\hat{\rho}_{Pf} = 0.1$ .

### 3.5.2.2 Temperature on concave outer surface

We complete the study of pedestal size effects by considering the situation where the hot temperature is applied on the concave outer surface of the system, as shown in Figs 14c-d. The reference of outer wall 1, and inner wall 2 is now inverted with respect to Figs 14a-b, while the combined structural constraint cases A-B, are applied in the same manner (described in Section 2.4). Instead of the effect of a missing pedestal, the scope here is to identify differences in the nature of pedestal stresses with respect to the case when temperature is applied on the convex outer surface of the system (Figs 18a-b), which has been analysed in detail throughout this manuscript. The fundamental difference in Figs 11c-d with respect to Figs 14a-b, is that the two cylindrical walls have the potential to approach each other in the radial,  $r$ , direction, imposing significant compressive forces through the pedestals; this effect is reproduced by the theoretical 2D analysis in Section 2.3.3, which is relevant to the current  $r - \theta$  plane.

combined effect of  $\hat{L}_{\theta,z} - \hat{D}_p$  on max stresses amongst pedestals, in the absence of a pedestal

temperature applied on convex outer surface

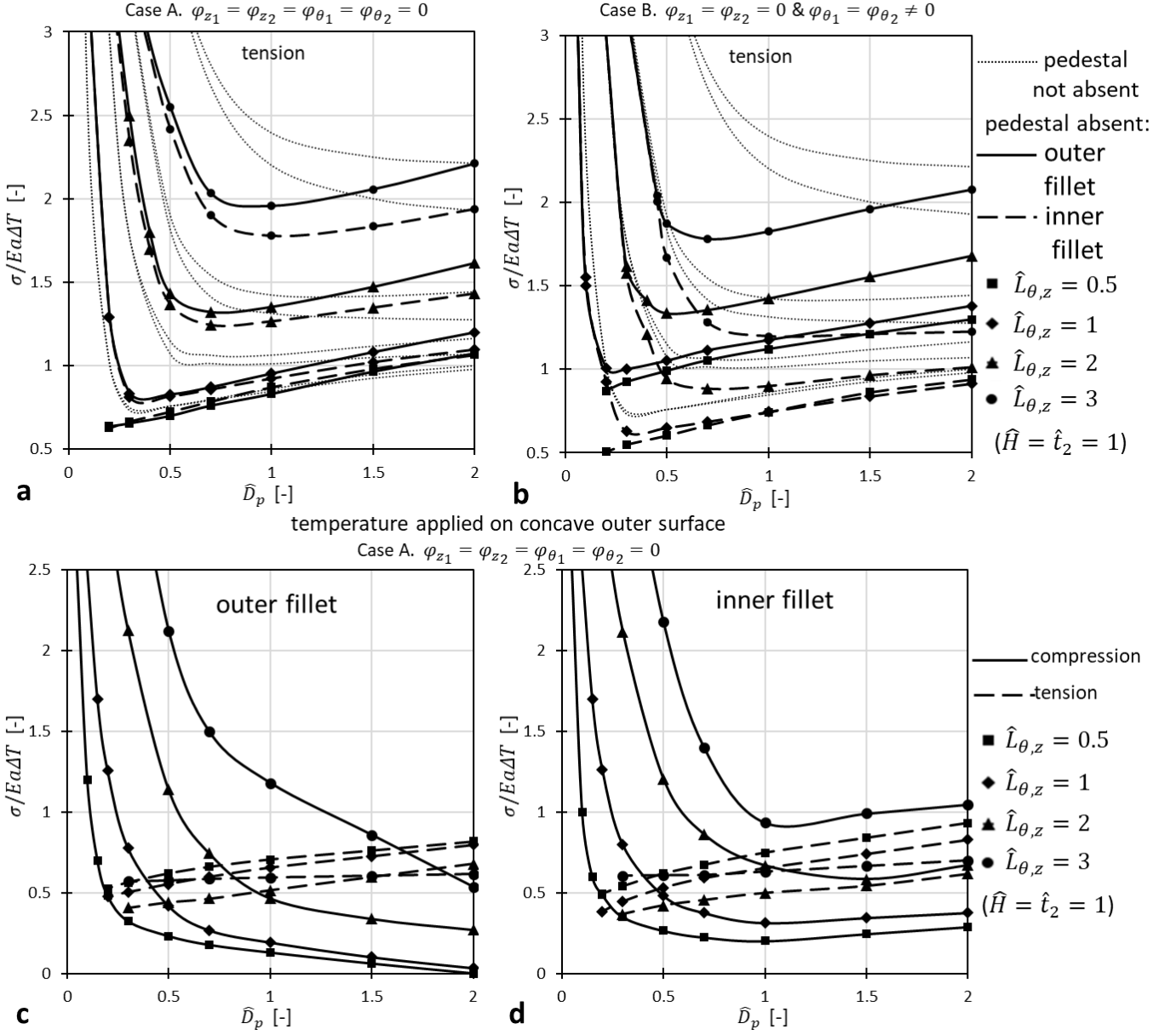


Figure 18. Combined effect of pedestal diameter,  $\hat{D}_p$  (circular section) and pedestal spacing,  $\hat{L}_{\theta,z}$ , on critical pedestal fillet stresses for the double wall system of Figs 14a-b where pedestals are periodically removed from the system. Plots show: (a-b) maximum pedestal tensile stresses for constraint cases A-B, when a hot temperature is applied on the convex outer wall surface (cases in Figs 14a-b) - corresponding results of the unit cell of Figs 8a-b (all pedestals present) are also plotted as dotted lines, and, (c-d) maximum compressive stresses and tensile stresses simultaneously occurring near the pedestal fillet when a hot temperature is applied on the concave outer wall surface (cases in Figs 14c-d), for case A only. Fixed geometric ratios include:  $\hat{R} = 20$ ,  $\hat{t}_2 = \hat{H} = 1$ , and  $\hat{\rho}_{Pf} = 0.1$ .

A consequence of this feature for both constraint cases A-B (Figs 14c-d), is a sharp transition of stress states at the pedestal fillets, from tensile states (associated with the inner surface of wall 1), into compressive states (associated with the bulk of the pedestals); the effect is more pronounced for case A, which is due to larger membrane forces in the walls, compared to case B, and thus larger compressive forces through the pedestals. The severity of the effect for case A is shown in Figs 18c-



d, through its effect on the variation of maximum outer fillet and inner fillet compressive and tensile stresses, over different pedestal spacings,  $\hat{L}_{z,\theta}$ , and pedestal sizes,  $\hat{D}_p$ . Here, the sharp stress increase below critical  $\hat{D}_p$  values occurs for the compressive states, while similar to Fig 18a the critical  $\hat{D}_p$  value increases with  $\hat{L}_{z,\theta}$ . Tensile fillet stresses (Figs 18c-d) are considerably lower than the corresponding stresses when a hot temperature is applied on the convex outer surface (Fig 18a), and furthermore, are shown to decrease with increasing  $\hat{L}_{z,\theta}$  (see Fig 18c-d). This decrease is consistent with our 2D analysis (Section 2.3.3) for the  $r - \theta$  plane, in that the bending moment,  $M_{\theta_1}$  (per unit length) decreases with increasing  $\hat{L}_{z,\theta}$  near the pedestal and increases away from the pedestal i.e. at  $\bar{\theta} = \bar{z} = 0$ . Evidently, for both cases A-B, Figs 14c-d indicate that both compressive and tensile stresses in the outer and inner wall 1 surfaces, increase away from the pedestals, especially at the effusion hole location,  $\bar{\theta} = \bar{z} = 0$ . The major role of inner wall thickness and wall spacing,  $\hat{t}_2 - \hat{H}$ , is expected to be similar to the case when a hot temperature is applied on the convex surface (Fig 16).

## 4 Conclusions

This study aims to cover all the essential aspects that determine the generation of thermal stresses in double wall transpiration cooling systems being considered for high temperature applications, such as hypersonic flight, gas turbine technologies and power generation. Such information is essential for the design of these systems for optimal thermomechanical and cooling performance.

Theoretical-FE 2D and 3D analyses indicate that the cases of externally constrained rotations in flat walls and self-constrained rotations in closed cylindrical walls produce similar thermoelastic 2D stress fields. These cases are inevitable in long cylindrical walls and therefore are suggested to be more representative for use in the design of self-connected wall geometries, such as double wall gas turbine blades. The stress field in the hot wall is caused by a bending moment that constraints the thermal curvature and a compressive membrane force arising by the thermal mismatch between the two walls and the fact that the walls must extend equally. The above cases differ from situations where the walls have free ends and therefore rotations are allowed. Here compressive stresses are much less severe and the stress field is caused by the fact that the walls must experience common rotations i.e. the thermal curvature of the hot wall is constrained by the presence of the cooler wall. These considerations explain the thermoelastic stress results of large scale 3D FE turbine blade models and smaller scale representative unit block models.

The presence of the inner cool wall generally increases the critical compressive stresses at the hot outer surface and decreases the tension at the inner surface of the outer wall, when compared to a single wall system. As the hot wall becomes thicker, its critical compressive stresses are reduced at the cost of increasing tension in the inner hot wall surface. For a hot wall with convex outer hot surface, increasing pedestal spacing can lead to excessive tension in the pedestal, whereas for a hot wall with a concave outer hot surface it can lead to extreme compression in the pedestal. Therefore, a lower bound in pedestal diameter must be used in design to avoid these overstress effects; this bound is a function of pedestal spacing, inner cool wall thickness and the wall geometric curvatures. A narrow pedestal height is generally beneficial, although its effect arises only when non-zero net rotations occur in the double wall system about at least one axis.

Wall thickness ratio is shown to be the critical parameter that should be tailored to maximise creep-fatigue performance. Ultimately this requires introducing effusion holes in the analysis,

material creep-plastic behaviour as well as considering thermal cycling conditions and inertial loading; we explore these aspects in subsequent papers. Our elastic analyses here provides the essential nominal stresses that drive actual stresses and localised plasticity effects at holes and pedestal fillets, and further, narrows drastically the range and number of case studies required to cover the above aspects, in order to finally deduce geometry-component life relationships.

## Acknowledgements

The authors acknowledge Dr Alex Murray and Prof Peter Ireland for useful discussions. This work was supported by EPSRC Programme Grant EP/P000878/1.

## APPENDIX – MPC subroutine of Section 2.4

Implementation of the ABAQUS MPC subroutine for enforcing nodes to lie within the same conical surface (Section 2.3.2), firstly requires decomposing the governing Equation (8) into:

$$(r_{1o} + u_{r1} - r_{2o} - u_{r2})(z_{1o} + u_{z1} - z_{io} - u_{zi}) + (z_{2o} + u_{z2} - z_{1o} - u_{z1})(r_{1o} + u_{r1} - r_{io} - u_{ri}) = 0 \quad (A1)$$

where  $r_{1o}$ ,  $z_{1o}$ ,  $r_{2o}$ ,  $z_{2o}$ ,  $r_{io}$ ,  $z_{io}$ , are original coordinates ( $r\theta z$  system) of the independent nodes, 1 and 2, and dependent node,  $i$ , and  $u_{r1}$ ,  $u_{z1}$ ,  $u_{r2}$ ,  $u_{z2}$ ,  $u_{ri}$ ,  $u_{zi}$ , are corresponding displacements. The MPC subroutine is essentially used to translate Equation (A1) into the linearized form:

$$dF = A^1 du^1 + A^2 du^2 + A^3 du^3 + A^4 du^4 = 0 \quad (A2)$$

which is applied in each FE analysis iteration, for each dependent node  $i$ . The vector,  $u^1 = (u_{zi})$ , includes the dependent degree of freedom (DOF) that is eliminated by the constraint, whereas  $u^2 = (u_{ri})$  represents the independent DOF of the dependent node,  $i$ ; vectors,  $u^3 = (u_{r1}, u_{z1})$ , and,  $u^4 = (u_{r2}, u_{z2})$ , include the (independent) DOFs of nodes 1, 2, respectively. Translation of Equation (A1) into (A2) relies here on providing the following derivative vectors:  $A^1 = (\partial F / \partial u_1^1) = (u_{r2} - u_{r1})$ ,  $A^2 = (\partial F / \partial u_1^2) = (u_{z1} - u_{z2})$ ,  $A^3 = (\partial F / \partial u_1^3, \partial F / \partial u_2^3) = (u_{z2} - u_{zi}, u_{ri} - u_{r2})$ , and  $A^4 = (\partial F / \partial u_1^4, \partial F / \partial u_2^4) = (u_{zi} - u_{z1}, u_{r1} - u_{ri})$ .

For dependent nodes,  $i$ , that lie at the unit cell corners (Fig 1c) i.e. the intersections of  $\bar{z} = 0$  with the symmetry planes  $\bar{\theta} = 0$  and  $\bar{\theta} = 1$ , the circumferential DOFs of each node,  $i$ , must be additionally constrained to zero. This firstly involves applying the boundary condition,  $u_{\theta 1} = u_{\theta 2} = 0$ , on the independent nodes, and thereafter coupling one of them with the DOF of node,  $i$ , i.e.  $u_{\theta i} - u_{\theta 1} = 0$ . In the MPC subroutine, this requires introducing an additional constraint equation,  $dG = B^1 du^1 + B^3 du^3 = 0$ , and instead using,  $u^1 = (u_{zi}, u_{\theta i})$ ,  $u^3 = (u_{r1}, u_{z1}, u_{\theta 1})$ , with  $B^1 = (\partial G / \partial u_1^1) = (1)$  and  $B^3 = (\partial G / \partial u_3^3) = (-1)$ ; the vectors  $u^2$ ,  $u^4$  and derivatives  $A^1$ ,  $A^2$ ,  $A^3$ ,  $A^4$  remain the same.

## REFERENCES

1. Thulin, R.D., D.C. Howe, and I.D. Singer, *Energy efficient engine high-pressure turbine detailed design report*. 1982.
2. Murray, A.V., *Advanced gas turbine cooling: double-wall turbine cooling technologies in turbine NGV/blade applications*. 2019, University of Oxford.
3. Cerminara, A., R. Deiterding, and N.D. Sandham, *Transpiration cooling using porous material for hypersonic applications*. *Convective Heat Transfer in Porous Media*, 2019: p. 263.
4. Murray, A.V., P.T. Ireland, and A.J. Rawlinson. *An Integrated Conjugate Computational Approach for Evaluating the Aerothermal and Thermomechanical Performance of Double-Wall Effusion Cooled Systems*. in *ASME Turbo Expo 2017: Turbomachinery Technical Conference and Exposition*. 2017. American Society of Mechanical Engineers Digital Collection.
5. Zhang, H., et al., *Effects of compound angle on film cooling effectiveness considering endwall lateral pressure gradient*. *Aerospace Science and Technology*, 2020: p. 105923.
6. Reed, R.C., *The superalloys: fundamentals and applications*. 2008: Cambridge university press.
7. Sweeney, P.C. and J.F. Rhodes, *An infrared technique for evaluating turbine airfoil cooling designs*. *J. Turbomach.*, 2000. **122**(1): p. 170-177.
8. Wang, C., J. Zhang, and J. Zhou, *Optimization of a fan-shaped hole to improve film cooling performance by RBF neural network and genetic algorithm*. *Aerospace Science and Technology*, 2016. **58**: p. 18-25.
9. Zamiri, A., S.J. You, and J.T. Chung, *Large eddy simulation of unsteady turbulent flow structures and film-cooling effectiveness in a laidback fan-shaped hole*. *Aerospace Science and Technology*, 2020: p. 105793.
10. Ngetich, G.C., et al., *A three-dimensional conjugate approach for analyzing a double-walled effusion-cooled turbine blade*. *Journal of Turbomachinery*, 2019. **141**(1).
11. Murray, A.V., et al., *High Resolution Experimental and Computational Methods for Modelling Multiple Row Effusion Cooling Performance*. *International Journal of Turbomachinery, Propulsion and Power*, 2018. **3**(1): p. 4.
12. Broomfield, R.W., et al., *Development and turbine engine performance of three advanced rhenium containing superalloys for single crystal and directionally solidified blades and vanes*. 1998.
13. Krewinkel, R., *A review of gas turbine effusion cooling studies*. *International Journal of Heat and Mass Transfer*, 2013. **66**: p. 706-722.
14. Kumar, S. and A. Cocks, *Sintering and mud cracking in EB-PVD thermal barrier coatings*. *Journal of the Mechanics and Physics of Solids*, 2012. **60**(4): p. 723-749.
15. Hermann, T.A., I. Naved, and M. McGilvray. *Performance of Transpiration Cooled Heat Shields for Hypersonic Vehicles*. in *AIAA Scitech 2019 Forum*. 2019.
16. Li, W., et al., *Wall thickness and injection direction effects on flat plate full-coverage film cooling arrays: Adiabatic film effectiveness and heat transfer coefficient*. *International Journal of Thermal Sciences*, 2019. **136**: p. 172-181.
17. Murray, A.V., P.T. Ireland, and E. Romero, *Development of a Steady-State Experimental Facility for the Analysis of Double-Wall Effusion Cooling Geometries*. *Journal of Turbomachinery*, 2019. **141**(4).
18. Han, J.-C., S. Dutta, and S. Ekkad, *Gas turbine heat transfer and cooling technology*. 2012: CRC press.
19. Funazaki, K., et al. *Heat Transfer Characteristics of an Integrated Cooling Configuration for Ultra-High Temperature Turbine Blades: Experimental and Numerical Investigations*. in *ASME Turbo Expo 2001: Power for Land, Sea, and Air*. 2001. American Society of Mechanical Engineers Digital Collection.

20. Skamniotis, C. and A.C. Cocks, *Minimising thermal stresses in double wall transpiration cooled components for high temperature applications*. International Journal of Mechanical Sciences, 2020: p. 105983.
21. Padture, N.P., M. Gell, and E.H. Jordan, *Thermal barrier coatings for gas-turbine engine applications*. Science, 2002. **296**(5566): p. 280-284.
22. Kim, K.M., et al., *Optimal design of impinging jets in an impingement/effusion cooling system*. Energy, 2014. **66**: p. 839-848.
23. Ponter, A. and S. Karadeniz, *An extended shakedown theory for structures that suffer cyclic thermal loading, Part 1: Theory*. 1985.
24. Karadeniz, S., A. Ponter, and K. Carter, *The plastic ratcheting of thin cylindrical shells subjected to axisymmetric thermal and mechanical loading*. 1987.
25. Sadowski, T. and P. Golewski, *Detection and numerical analysis of the most efforted places in turbine blades under real working conditions*. Computational Materials Science, 2012. **64**: p. 285-288.
26. Rauch, M., et al., *Life assessment of multiaxially cyclic loaded turbine components*. 2008. **31**(6): p. 441-451.
27. Chen, L.J., Y.H. Liu, and L.Y. Xie, *Power-exponent function model for low-cycle fatigue life prediction and its applications - Part II: Life prediction of turbine blades under creep-fatigue interaction*. International Journal of Fatigue, 2007. **29**(1): p. 10-19.
28. Tang, W., et al., *Numerical simulation of temperature distribution and thermal-stress field in a turbine blade with multilayer-structure TBCs by a fluid-solid coupling method*. Journal of Materials Science & Technology, 2016. **32**(5): p. 452-458.
29. Elmukashfi, E.M.A., et al., *Analysis of the Thermomechanical Stresses in Double-Wall Effusion Cooled Systems*. Journal of Turbomachinery: p. 1-15.
30. Albiñana, J. and C. Vila, *A framework for concurrent material and process selection during conceptual product design stages*. Materials & Design, 2012. **41**: p. 433-446.
31. Systèmes, D., *Abaqus*. Providence, RI: Dassault Systèmes.[Google Scholar], 2016.
32. Cocks, A.C.F., *Lower-Bound Shakedown Analysis of a Simply Supported Plate Carrying a Uniformly Distributed Load and Subjected to Cyclic Thermal Loading*. International Journal of Mechanical Sciences, 1984. **26**(9-10): p. 471-475.
33. Ponter, A. and S. Karadeniz, *An extended shakedown theory for structures that suffer cyclic thermal loading, Part 2: applications*. 1985.
34. Halford, G., M. Hirschberg, and S. Manson, *Creep fatigue analysis by strain-range partitioning*. 1971.
35. Darveaux, R. and K. Banerji, *Fatigue analysis of flip chip assemblies using thermal stress simulations and a Coffin-Manson relation*. in *1991 Proceedings 41st Electronic Components & Technology Conference*. 1991. IEEE.
36. Kim, K.M., et al., *Thermo-mechanical life prediction for material lifetime improvement of an internal cooling system in a combustion liner*. Energy, 2011. **36**(2): p. 942-949.
37. Cocks, A.C.F. and A.R.S. Ponter, *Creep Deformation and Failure under Cyclic Thermal Loading*. Nuclear Engineering and Design, 1989. **116**(3): p. 363-387.
38. Zhu, S.-P., et al., *A combined high and low cycle fatigue model for life prediction of turbine blades*. Materials, 2017. **10**(7): p. 698.
39. Chen, H. and A.R. Ponter, *Shakedown and limit analyses for 3-D structures using the linear matching method*. International Journal of Pressure Vessels and Piping, 2001. **78**(6): p. 443-451.
40. Chen, L., Y. Liu, and L. Xie, *Power-exponent function model for low-cycle fatigue life prediction and its applications—Part II: Life prediction of turbine blades under creep-fatigue interaction*. International journal of fatigue, 2007. **29**(1): p. 10-19.
41. Liu, H., et al., *A numerical approach to simulate 3D crack propagation in turbine blades*. International Journal of Mechanical Sciences, 2020. **171**: p. 105408.

42. Carter, T.J., *Common failures in gas turbine blades*. Engineering Failure Analysis, 2005. **12**(2): p. 237-247.
43. Hong, H., W. Wang, and Y. Liu, *High-temperature fatigue behavior of a steam turbine rotor under flexible operating conditions with variable loading amplitudes*. International Journal of Mechanical Sciences, 2019. **163**: p. 105121.
44. Banaszkiewicz, M., *Numerical investigations of crack initiation in impulse steam turbine rotors subject to thermo-mechanical fatigue*. Applied Thermal Engineering, 2018. **138**: p. 761-773.
45. Cunha, F., M. Dahmer, and M. Chyu. *Thermal-Mechanical Life Prediction System for Anisotropic Turbine Components*. in *Turbo Expo: Power for Land, Sea, and Air*. 2005.
46. Dixon, S.L. and C. Hall, *Fluid mechanics and thermodynamics of turbomachinery*. 2013: Butterworth-Heinemann.
47. Scholz, A., et al., *Modeling of mechanical properties of alloy CMSX-4*. Materials Science and Engineering: A, 2009. **510**: p. 278-283.
48. Quested, P., et al., *Measurement and estimation of thermophysical properties of nickel based superalloys*. Materials Science and Technology, 2009. **25**(2): p. 154-162.
49. Rauch, M. and E. Roos, *Life assessment of multiaxially cyclic loaded turbine components*. Fatigue & Fracture of Engineering Materials & Structures, 2008. **31**(6): p. 441-451.
50. Yang, L., et al., *Finite element simulation on thermal fatigue of a turbine blade with thermal barrier coatings*. Journal of Materials Science & Technology, 2014. **30**(4): p. 371-380.
51. XiaoAn, H., et al., *Viscoplastic analysis method of an aeroengine turbine blade subjected to transient thermo-mechanical loading*. International Journal of Mechanical Sciences, 2019. **152**: p. 247-256.
52. Timoshenko, S.P. and J. Goodier, *Theory of elasticity*. 2011.
53. Skamniotis, C. and A.C. Cocks, *Designing against severe effusion hole stresses in double wall transpiration systems for high temperature applications* under review in Aerospace Science and Technology, 2021.
54. Timoshenko, S.P. and S. Woinowsky-Krieger, *Theory of plates and shells*. 1959: McGraw-hill.
55. Skamniotis, C. and A.C. Cocks, *Minimising stresses in double wall transpiration cooled components for high temperature applications*. International Journal of Mechanical Sciences, 2020. **189**: p. 105983.